Central Lancashire Online Knowledge (CLoK)

Title	Spiral arm kinematics for Milky Way stellar populations
Type	Article
URL	https://clok.uclan.ac.uk/19609/
DOI	https://doi.org/10.1093/mnras/stw1465
Date	2016
Citation	Pasetto, S, Natale, Giovanni, Kawata, D, Chiosi, C, Hunt, J.A.S and Brogliato, C (2016) Spiral arm kinematics for Milky Way stellar populations. Monthly Notices of the Royal Astronomical Society, 461 (3). pp. 2383-2409. ISSN 0035-8711
Creators	Pasetto, S, Natale, Giovanni, Kawata, D, Chiosi, C, Hunt, J.A.S and Brogliato, C

It is advisable to refer to the publisher's version if you intend to cite from the work.
https://doi.org/10.1093/mnras/stw1465

For information about Research at UCLan please go to http://www.uclan.ac.uk/research/

Spiral arm kinematics for Milky Way stellar populations

S. Pasetto,[1]★ G. Natale,[2] D. Kawata,[1] C. Chiosi,[3] J. A. S. Hunt[1] and C. Brogliato[4]

[1]*Department of Space & Climate Physics, Mullard Space Science Laboratory, University College London, Holmbury St. Mary, Dorking, Surrey RH5 6NT, UK*
[2]*Jeremiah Horrocks Institute, University of Central Lancashire, Preston PR1 2HE, UK*
[3]*Department of Physics & Astronomy,'Galileo Galilei', University of Padua, I-35122 Padua, Italy*
[4]*Clover-lab, Valene rd, Salo, I-25087 Brescia, Italy*

ABSTRACT

We present a new theoretical population synthesis model (the Galaxy model) to examine and deal with large amounts of data from surveys of the Milky Way and to decipher the present and past structure and history of our own Galaxy. We assume the Galaxy to consist of a superposition of many composite stellar populations belonging to the thin and thick discs, the stellar halo and the bulge, and to be surrounded by a single dark matter halo component. A global model for the Milky Way's gravitational potential is built up self-consistently with the density profiles from the Poisson equation. In turn, these density profiles are used to generate synthetic probability distribution functions (PDFs) for the distribution of stars in colour–magnitude diagrams (CMDs). Finally, the gravitational potential is used to constrain the stellar kinematics by means of the moment method on a (perturbed)-distribution function. Spiral arms perturb the axisymmetric disc distribution functions in the linear response framework of density-wave theory where we present an analytical formula of the so-called 'reduction factor' using hypergeometric functions. Finally, we consider an analytical non-axisymmetric model of extinction and an algorithm based on the concept of probability distribution function to handle CMDs with a large number of stars. A genetic algorithm is presented to investigate both the photometric and kinematic parameter space. This galaxy model represents the natural framework to reconstruct the structure of the Milky Way from the heterogeneous data set of surveys such as *Gaia*-ESO, SEGUE, APOGEE2, RAVE and the *Gaia* mission.

Key words: surveys – Hertzsprung–Russell and colour-magnitude diagrams – ISM: kinematics and dynamics – Galaxy: fundamental parameters – Galaxy: kinematics and dynamics – Galaxy: structure.

1 INTRODUCTION

The Milky Way (MW) provides a unique environment in which to study the origin and evolution of galaxies on a star-by-star basis, with a precision that is simply impossible to reach for any other galaxy in the Universe. The European Space Agency's cornerstone mission *Gaia*, together with complementary ground-based spectroscopic follow-ups such as the *Gaia*-ESO Survey (e.g. Gilmore et al. 2012), will map the stellar distribution of the MW with unprecedented accuracy by providing high-precision phase-space information, physical parameters, and chemical compositions, for roughly one billion of the stars in our Galaxy. The exploitation of this huge amount of data cannot be made using the methods and tools that have been used for many decades to study much less numerous samples of stars; it requires the development of, and experience with, cutting-edge multidimensional data mining tools, as well as

sophisticated methodologies to transfer the models from the space of 'simulations' to the 'plane of observers'.

Star-count techniques are born with the aim to answer a simple astronomical question: why do we see a given distribution of stars in the sky? Since the oldest approach to the star-count equation (e.g. Trumpler & Weaver 1953), these techniques have represented the most natural way to investigate the closest distribution of stars to us, i.e. the MW. A major advancement of these techniques was achieved by Bahcall & Soneira (1984) who applied the concept of stellar populations to the solar neighbourhood (see also Bahcall 1984a,b) and nowadays, more theoretically sophisticated star-count models are the standard tools to investigate the MW stellar distribution (e.g. the Besançon model; Robin et al. 2003). The ultimate step towards the understanding of our Galaxy is thus represented by the extension of the concept of stellar populations to include kinematics, dynamics, photometric and chemical properties together in a global MW modelling approach (e.g. Méndez et al. 2000; Vallenari et al. 2006). The star-count techniques have the goal to synthetically reproduce the observables obtained from an (unknown)-stellar

distribution function (DF), i.e. the number of stars in a given range of, e.g. temperature, velocities, densities, proper motions etc., by considering the data distribution in the space of the observable quantities (e.g. photometry, proper motions, radial velocities, etc.). To achieve this goal, a number of founding pillars must be assumed to exist on a global scale, e.g. density-profile laws, star formation histories, age–metallicity relations, age–velocity dispersion relations etc. All these relations will ultimately represent a way of deciphering and constraining the MW history and evolution.

The more independent constraints a model can reproduce, the closer these underlying relations are to the true properties of the system analysed (the MW in our case). The star-count techniques are a Monte Carlo type solution to a multidimensional integration problem of the star-count equation. Historically, in classical textbooks of statistical astronomy (Trumpler & Weaver 1953) the star-count equation is generalized to include the kinematics as follows:

$$\frac{\mathrm{d}N_j}{\mathrm{d}\boldsymbol{\gamma}\,\mathrm{d}m_{\Delta\lambda}\mathrm{d}C_{\lambda\lambda'}} = N_j f_j(\boldsymbol{\gamma}), \tag{1}$$

where N_j is the number of stars for each given stellar population, j, with DF $f_j(\boldsymbol{\gamma})$ in the elemental volume of the phase space $d\boldsymbol{\gamma} = \{\mathrm{d}\boldsymbol{x}, \mathrm{d}\boldsymbol{v}\} = \{\mathrm{d}\,\widehat{\Omega}\,\mathrm{d}r_{\mathrm{hel}}, \mathrm{d}\boldsymbol{v}\}$. Here, r_{hel} is the heliocentric distance of the stars in an infinitesimal interval of magnitude $\mathrm{d}m_{\Delta\lambda}$ in the band $\Delta\lambda$ and colour $\mathrm{d}C = m_{\Delta\lambda} - m_{\Delta\lambda'}$, $\mathrm{d}\,\widehat{\Omega} = \mathrm{d}l\mathrm{d}b\cos b$ (with l and b Galactic longitude and latitude) is the solid angle. In Section 2, we will review a generalized framework for equation (1) introduced in Pasetto, Chiosi & Kawata (2012b) to recover equation (1) as a special case of a multidimensional marginalization process.

Two of the major limitations underlying many theoretical works based on analytical expressions for the DF $f_j(\boldsymbol{\gamma})$ are the time independence of f_j and its axisymmetry properties in the configuration space. Related to the first assumption is the problem of self-consistency: the DFs are not obtained by sampling the phase-space of a system evolved in time under the effect of self-gravity. In this approach, the DF is not numerical but a parametric function. The second assumption of axisymmetry is led by the necessity to keep the treatment of the dynamical evolutions as simple as possible: the corresponding Hamiltonian is cyclic in some variables and hence more suited for analytical manipulation.

The literature is full of alternatives to overcome these two limitations, e.g. *N*-body simulations, the Schwarzschild method, the made-to-measure method, full theoretical methods (e.g. Cubarsi 2007; Bienaymé & Traven 2013; Hunt & Kawata 2013; Bienaymé, Robin & Famaey 2015; Hunt et al. 2015) etc., whose review is beyond the goal of this paper. In this work, we will relax the axisymmetry assumption for the sole thin disc components by implementing a perturbative approach carried out to the linear order on suitable small parameters to the equation of motion following two different works by Lin, Yuan & Shu (1969) and Amendt & Cuddeford (1991). These perturbative linear response frameworks are the only analytical treatment available up to now that can claim observational validation.

The perturbative treatment of Amendt & Cuddeford (1991) deals with mirror symmetries about the plane of the Galaxy. It has been introduced in the technique we are adopting from Pasetto PhD thesis 2005 (e.g. Vallenari et al. 2006) where more detail has been given as well as comments about its implementation and observational validation. Nowadays, this work represents a good balance between simplicity and robustness. More recent formulations can be investigated in the future (e.g. Bienaymé 2009).

The treatment of Lin et al. (1969) is referred as density-wave theory (DWT) and we will review in what follows the literature that attempts to validate it from the observational point of view.

The history of the attempts to find an explanation of the spiral features of the MW and external galaxies is long standing and still matter of debate. We recall here (without the presumption to be complete) a few works of observational nature that inspired our star-count implementation of DWT. The interested reader can look at books such as Shu (1991) or Bertin (2014).

1.1 Observational studies of DWT

The existence of a theory interpreting the spiral arm phenomenon (e.g. Lin & Shu 1964; Marochnik 1964, 1966, 1967; Marochnik & Ptitsina 1968; Lin et al. 1969; Marochnik & Suchkov 1969a,b) spurred many research groups to find observational evidence that could either support or deny such a theory. The first attempt to interpret the mean properties of observational velocity fields of young stars in terms of the DWT was by Creze & Mennessier (1973). Creze & Mennessier (1973) set up a method to interpret the observations in terms of the DWT based on two simple ingredients: a multidimensional parametric fit and an asymptotic expansion on small parameters of the basic equations governing the kinematics of the DWT. This seminal study inspired many other studies in which different results were obtained mainly due to either the adopted multidimensional fitting procedure or the large number of involved parameters or the different data sets in usage and their local/non-local nature in the configuration space. Local models of the velocity space have been considered with asymptotic expansions on different small parameters (e.g. Nelson & Matsuda 1977; Brosche & Schwan 1981; Byl & Ovenden 1981; Comeron & Torra 1991; Mishurov et al. 1997; Mishurov & Zenina 1999; Fernández, Figueras & Torra 2001; García-Sánchez et al. 2001).

Nowadays this research is still far from being complete (see e.g. Griv, Ngeow & Jiang 2013; Junqueira et al. 2013; Griv et al. 2014; Roca-Fàbrega et al. 2014; Vallée 2014, 2016b). Recent studies consider more complex models based on four spiral arms (e.g. Lépine, Mishurov & Dedikov 2001; Vallée 2016a) and their connections with the pattern of chemical properties of the MW (e.g. Lépine, Acharova & Mishurov 2003; Andrievsky et al. 2004) and the not monotonic features of the MW rotation curve (e.g. Barros, Lépine & Junqueira 2013). Finally, this research field has been recently boosted by numerical simulations. *N*-body solvers are achieving higher and higher resolution and although they are still missing a complete self-consistent understanding of the spiral arm dynamics, several numerical techniques (e.g. the tree-code; Barnes & Hut 1986) allow us to simulate the gravitational interactions among millions of particles with masses of the order of a few thousand solar masses or less (Grand, Kawata & Cropper 2012a,b; D'Onghia, Vogelsberger & Hernquist 2013).

The logic flux of the paper is as follows. We first want to present (Section 2) the concept of stellar population taken from a theory developed in its general form in Pasetto et al. (2012b) and here adapted to the specific case of the MW stellar populations. This will allow us to generalize the previously introduced concept of star-counts in a larger theoretical framework, to set a few assumptions, and to emphasize the goals of this novel Galaxy model. We present the normalization of the star-count equation for a field of view (FOV) of arbitrary size in Section 3 and this allows us to define the density profiles and the consequent MW potential shape (Section 4). This axysimmetric potential represents the basis for the development of a self-consistent spiral treatment presented in the following section,

Table 1. Meridional plane profile of the velocity ellipsoid. For each fixed radius, the vertical gradient of the two velocity dispersion tensors is indicated in the fourth and fifth columns. The third column gives the vertical ranges.

j	z_j (kpc)	Δz (kpc)	$\frac{\partial \sigma_{RR}}{\partial z}, \frac{\partial \sigma_{zz}}{\partial z}$ (km s^{-1} kpc^{-1})
0	$z_0 = 0.0$	$|z| = 0$	0.0,0.0
I	$z_1 = 0.5$	$|z| \in\ ]0.0, 0.5]$	27.2,17.4
II	$z_2 = 1.0$	$|z| \in\ ]0.5, 1.0]$	9.7,5.4
III		$|z| > 1.0$	0.0,0.0

but as explained above, the formulation adopted in our approach is fully analytical, hence parametric, and so are the density-potential couple introduced in Section 4. This leaves us with a large number of parameters to deal with in order to model the MW. In Section 5, a genetic algorithm is introduced for the study of these parameters which are used to study the MW data surveys. This leads us to the setting of the MW axisymmetric potential (Table 1) that represents the axysimmetric basis used to develop the spiral arms perturbation theory. Hence, in Section 6 the spiral arms formalism is presented with its implication for the density (Section 6.1) and the colour–magnitude diagrams (CMDs; Section 6.2) once an ad hoc extinction model is considered (Section 6.2.1). The velocity field description is presented in Section 7. A direct comparison with the most popular Besançon model is detailed in Section 8 and the conclusions are presented in Section 9.

2 THEORY OF STELLAR POPULATIONS

Robust mathematical foundations for the concept of stellar populations are still missing, but recently Pasetto et al. (2012b) proposed a new formulation for it. We briefly summarize here the analysis of Pasetto et al. (2012b) because it is the backbone of the population synthesis model we are going to describe here. This approach extends the classical concepts presented in books as Salaris & Cassisi (2005) or Greggio & Renzini (2011) to include a phase-space treatment for the stellar populations. These definitions will be crucial for the modelling approach and to formally define our goals. Moreover they will allow us to fix some assumptions we exploited during our work. Hence, we proceed to pin down here the more specific points that in the theory proposed in Pasetto et al. (2012b) are introduced in complete generality.

2.1 Theoretical framework: $\mathbb{E}_{MW}$

We define every assembly of stars born at different time, positions, with different velocities, masses and chemical composition a composite stellar population (CSP). The space of existence for the MW CSP, $\mathbb{E}_{MW}$ is considered as the Cartesian product of the phase-space $\mathbf{\Gamma} = (x_1, x_2, \ldots, x_{3N}, v_1, v_2, \ldots, v_{3N})$ (N number of stars of the CSP), the mass space M, and the chemical composition space Z, $\mathbb{E}_{MW} \equiv M \times Z \times \mathbf{\Gamma}$. The inclusion of the time t introduces the 'extended'-existence space $\mathbb{E}_{MW} \times \mathbb{R}$. A more formal geometrical definition of this space and its dimensionality for the interested reader is given in Pasetto et al. (2012b). Because in the extended existence space the MW stars move continuously (losing mass, enriching in metals and travelling orbits in the phase-space), we can safely define a distribution for the CSP in $\mathbb{E}_{MW}$, say $f_{CSP}^{MW} \in \mathbb{R}^+$ real always positive function under the assumption of continuity and differentiability, i.e. $f_{CSP}^{MW} \in C^\infty(\mathbb{R}^+)$. We consider now a sample of
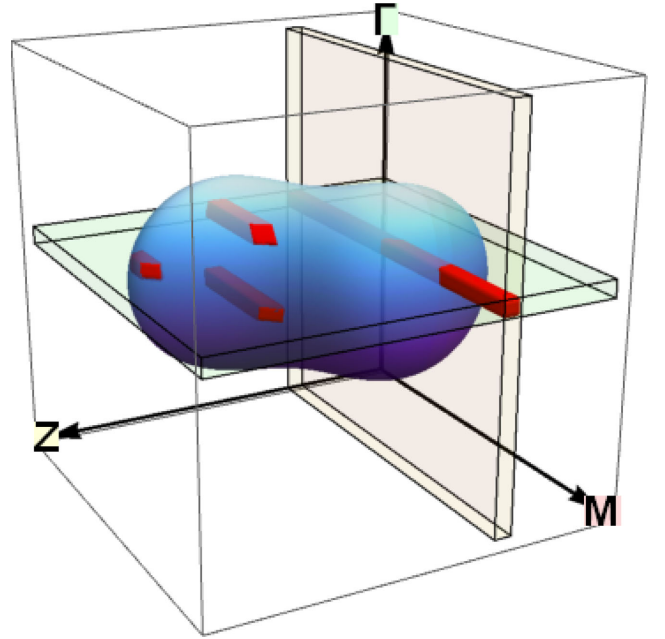

Figure 1. Cartoon representing the concept of a foliation of a CSP over SSPs. SSPs result as an intersection (red rectangular area in the figure) of planes of constant metallicity dZ (light-brown-colour) and constant phase-space d$\mathbf{\Gamma}$ plane (light-green colour) with the CSP (blue). The SSPs are the fundamental 'atoms' to build up the CSPs. Axes are in arbitrary units.

identical MW-systems whose initial condition spans a subvolume of $\mathbb{E}_{MW}$, let us refer to it as the 'MW-ensemble'. The number of these systems, dN, spanning a mass range, dM, a metallicity range, dZ, and phase-space interval, d$\mathbf{\Gamma}$, at the instant t, is given by

$$\mathrm{d}N = N f_{CSP}^{MW} \mathrm{d}M \mathrm{d}Z \mathrm{d}\mathbf{\Gamma}, \tag{2}$$

and the total number of systems in the ensemble is fixed, finite, and subject to the important normalization condition

$$\int_{\mathbb{E}_{MW}} f_{CSP}^{MW} \mathrm{d}M \mathrm{d}Z \mathrm{d}\mathbf{\Gamma} = 1. \tag{3}$$

Pasetto et al. (2012b) proceeded with a foliation of $\mathbb{E}_{MW}$ in orthogonal subspaces of metallicity, dZ, and phase-space alone, d$\mathbf{\Gamma}$, to define a simple stellar population (SSP) as one of these elemental units. A cartoon of the concept of SSPs is presented in Fig. 1.

As evident, we can assume that the DF of a CSP can be written as the sum of disjoined DF of SSP,

$$f_{CSP}^{MW} = \sum_{SSP=1}^{n} f_{SSP}, \tag{4}$$

where $f_{SSP} = f_{SSP}(M, Z_0, \mathbf{\Gamma}_0; t_0)$ is the DF of a single stellar population born at time t_0. In this framework, we can give a rigorous geometrical interpretation and definition of CSPs and SSPs (see Pasetto et al. 2012b). This number is related to the granularity of f_{CSP}^{MW} and hence to the growth of the entropy of the MW as a whole. The study of the number of SSPs is beyond the scope of this paper and here we will limit n to be a fixed parameter for simplicity. Further considerations on this number are left in Section 5 in relation to the machine learning approach used to study a given set of observations. As the time passes, the stellar population evolves. According to their masses the stars leave the main sequence (MS) and soon after die (supernovae phase) or enter into quiescent stages (white dwarfs phase) injecting chemically processed material into

the interstellar medium (ISM) in form of supernovae remnants or winds. In the same way, the evolution of an SSP in the phase-space obeys the Liouville equation $\frac{\partial f_\Gamma}{\partial t} = -\iota \mathcal{L}[f_\Gamma]$ with $\mathcal{L}[*]$ Liouville operator and ι imaginary units.

It is of interest for us to recall a few tools which are useful in studying the MW. Within this framework, we will make use of the following concepts.

(i) *Present-day mass function.* This is the result of the marginalization of $f_{\mathrm{CSP}}^{\mathrm{MW}}$ over the metallicity Z and phase space $\mathbf{\Gamma}$:

$$\int_{\mathbb{R}^{6N} \times \mathbb{R}} N f_{\mathrm{CSP}}^{\mathrm{MW}} \mathrm{d}Z \mathrm{d}\mathbf{\Gamma} = \hat{\xi}(M; t). \tag{5}$$

This can be expressed, e.g. by the approximate relation

$$\hat{\xi}(M; t) = \begin{cases} \xi(M) \frac{t_{\mathrm{MS}}}{\tau} & t_{\mathrm{MS}} < \tau \\ \xi(M) & t_{\mathrm{MS}} > \tau, \end{cases} \tag{6}$$

where $\tau = t - t_0$ is the age of the stellar population, $t_{\mathrm{MS}} = t_{\mathrm{MS}}(M)$ is the age at which a star exits the MS, and $\xi(M)$ is the initial mass function (IMF) of the MS stars. In our model, the form of the IMF profiles is limited to multisegmented power laws and lognormal formula to cover most of the literature. All the IMFs matching a single/multi power-law family of models of the form $\xi(M)\mathrm{d}M = \xi_0 (\frac{M}{M_\odot})^{-\alpha} \frac{\mathrm{d}M}{M_\odot}$ (e.g. Salpeter 1955; Kroupa, Tout & Gilmore 1993; Kroupa 2001) are considered as well as the lognormal family of profiles $\xi(M)\mathrm{d}M = \xi_0 M^{-1} \mathrm{e}^{-\frac{1}{2\sigma_M^2}(\log \frac{M}{M_{\mathrm{min}}})^2} \frac{\mathrm{d}M}{M_\odot}$ (e.g. Chabrier 2003) where ξ_0, M_{min} and σ_M are free parameters.

(ii) *Age–metallicity relation.* By integration of the DF over the mass, M, and the phase-space, $\mathbf{\Gamma}$, we can define the relation,

$$\int_{\mathbb{R}^{6N} \times \mathbb{R}} N f_{\mathrm{CSP}}^{\mathrm{MW}} \mathrm{d}\mathbf{\Gamma} \mathrm{d}M = \chi(Z; t), \tag{7}$$

which gives the number of stars formed per metallicity interval at the time t. Although several studies have been devoted to investigate the age–metallicity relation (Pilyugin & Edmunds 1996; Rocha-Pinto et al. 2000, 2006), the small volume of the Galaxy covered by the data does not allow us to apply these age–metallicity relationships to a global scale model (Bergemann et al. 2014). The problem becomes even more puzzling for specific stellar components such as the stellar halo (see e.g. Leaman, VandenBerg & Mendel 2013, for the globular cluster case). Even though the age–metallicity relation of Rocha-Pinto et al. (2006) is included in our model, we will not use it as a standard assumption.

(iii) *Phase-space DF and age–velocity dispersion relation.* By marginalizing $f_{\mathrm{CSP}}^{\mathrm{MW}}$ over the mass and metallicity subspace we can write the formal relation,

$$\int_{\mathbb{R}^2} M f_{\mathrm{CSP}}^{\mathrm{MW}} \mathrm{d}M \mathrm{d}Z = \mathrm{e}^{-\iota \mathcal{L}t} f_\Gamma(\mathbf{\Gamma}; t_0), \tag{8}$$

whose analysis within the framework of a perturbative approach of the DWT will be subject of this paper in the following sections. Here, we anticipate only that by taking the moments on the velocities of equation (8) we can obtain the important *age–velocity* dispersion relation implemented in our model:

$$\sigma_v(\mathbf{x}; t) \equiv \int_{\mathbb{R}^{3N}} d^{3N} \mathbf{v} (\mathbf{v} - \bar{\mathbf{v}})^{\otimes 2} \int_{\mathbb{R}^2} M f_{\mathrm{CSP}}^{\mathrm{MW}} \mathrm{d}M \mathrm{d}Z$$
$$= \int_{\mathbb{R}^{3N}} (\mathbf{v} - \bar{\mathbf{v}})^{\otimes 2} \mathrm{e}^{-\iota \mathcal{L}t} f_\Gamma(\mathbf{\Gamma}; t_0) d^{3N} \mathbf{v}, \tag{9}$$

with $\mathbf{a}^{\otimes n}$ a standard tensor n-power of the generic vector $\mathbf{a}$ accounted for its symmetries. A simplified version of this relation

for a collisionless stellar system (i.e. where the Liouville operator introduced above is replaced by the Boltzmann operator for collisionless stellar dynamics) are implemented in our model with data interpolated from the values of the work of Pasetto et al. (2012d) and Rocha-Pinto et al. (2004, see equation 17).

Finally, by extension of the previous integral formalism of equations (5), (7) and (8) we introduce the following relations of interest to us.

(i) *Metallicity/phase-space relationship.* This relation is formally defined by $\eta(Z, \mathbf{\Gamma}; t) \equiv \int f_{\mathrm{CSP}}^{\mathrm{MW}} \mathrm{d}M$ and more interestingly we can project it on to the configuration space:

$$\hat{\eta}(Z, \mathbf{x}; t) = \int_{\mathbb{R}^{3N} \times \mathbb{R}} f_{\mathrm{CSP}}^{\mathrm{MW}} d^{3N} \mathbf{v} \mathrm{d}M. \tag{10}$$

There is indeed observational evidence of the presence of this relation in the chemical radial gradients in the configuration space of the MW thin disc component (see e.g. Boeche et al. 2013, 2014) and it can be eventually implemented on the thick disc (Curir et al. 2014).

For completeness, we remind the reader that the stellar-mass/metallicity relation can easily be defined and implemented in our model as presented in Pasetto et al. (2012b) once a larger sample of asteroseismology data becomes available (see references in Section 1).

The goal of our research is to develop a technique to investigate $\mathbb{E}_{\mathrm{MW}}$, the existence space of the MW, through the relations that result from the projection of the unknown $f_{\mathrm{CSP}}^{\mathrm{MW}}$ in the mentioned subspaces of equations (6), (7), (8) and (10).

To this aim, we need to relate $\mathbb{E}_{\mathrm{MW}}$ to the space of observations. This is made possible by the star-count equation, equation (1), in combination with equation (2) in the space of the observational data. To this aim, one has also to solve a crucial point of difficulty with equation (1), i.e. the large fields of view that are often involved.

3 STAR-COUNT EQUATION FOR LARGE SKY COVERAGE

Nowadays and increasingly in the future, we face the challenge of large sky coverage surveys where the gradients of the underlying MW stellar density distributions sensibly vary across the covered survey area. Already large surveys (SDSS, RAVE, SEGUE, etc.) present these characteristics, and the ongoing whole sky survey by *Gaia*, due to the depth of the magnitude limit and the amplitude of the solid angle considered ($\mathrm{d}\widehat{\Omega} = 4\pi$), will provide us an enormous amount of data to be considered. If a survey spans a large solid angle $\mathrm{d}\widehat{\Omega}$ and has a very deep magnitude limit, then the number of stars per FOV becomes large and its realization on a star-by-star basis becomes unpractical. For example, the marginalization of a $f_{\mathrm{CSP}}^{\mathrm{MW}}$ over $\mathrm{d}\mathbf{\Gamma}$ for large-scale survey data produces a section over $\mathrm{d}Z \times \mathrm{d}M$, i.e. a Hertzsprung–Russel or a CMD that can be over-dense: to realize it graphically we should draw dots-over-dots and count them. This process should be repeated every time we change a single parameter to see the effect of the variation until suitable fitting is achieved. To surpass these CMD realization problems, Pasetto et al. (2012b) presented a novel technique able to substitute the generation of synthetic stars with the computing of a probability distribution function (PDF). The convolution of several SSPs along a line of sight (l.o.s.), thanks to equation (4), was then substituting the Monte Carlo generation of stars for an FOV, de-facto changing the concept of a 'star-count' model with a PDF model.

We adopted here the same technique to speed up the generation of the $f_{\rm CSP}^{\rm MW}$, eventually walking back to a star-count type of model by populating the PDF obtained for $f_{\rm CSP}^{\rm MW}$ only if required. The stellar SSP data base used to build the $f_{\rm CSP}^{\rm MW}$ is the same adopted in Pasetto et al. (2012b), though any other SSP data base can be easily implemented virtually making the modelling approach independent of any particular stellar physics recipes adopted by one or another research group (rotation, overshooting, α-enhancement, helium enrichment etc.). More details of this is described for the interested reader in Pasetto et al. (2012b).

Nevertheless, this process of populating the PDF for each FOV (that can be as large as the full sky) has to be treated with attention because of the normalization relation (equation 3). In particular, the number of stars generated along the l.o.s. and appearing in the final CMD has to correctly account for the underlying mass fraction of each stellar component j of the Galaxy.

Historically, to deal with equation (1), or its generalized form in equation (2), the approach was based on the sum of several close FOV of negotiable opening angle. It was required for $d\widehat{\Omega}$ to be very small as well as the number of stars per population N_j. The result of these assumptions was that the underlying density distributions within $d\widehat{\Omega}$ were to a good approximation constant (if the survey was not too deep in magnitude and hence $r_{\rm hel}$ not too deep). To solve the star-count equation under these approximations was a trivial exercise and in the past decades it has been indeed done by several works in this research area (e.g. Méndez et al. 2000; Ng et al. 2002; Girardi et al. 2005; Robin et al. 2003; Vallenari et al. 2006, and references therein). If the hypothesis of small $d\widehat{\Omega} = dldb\cos b$ is to be relaxed, the computing of this number has to be performed numerically as follows:

$$
\begin{aligned}
N &= \int_{\mathbb{R}^{3N}} d^{3N}\boldsymbol{x} \int_{\mathbb{R}^{3N}} d^{3N}\boldsymbol{v} \int_{\mathbb{R}^2} M f_{\rm CSP}^{\rm MW}(M, Z, \boldsymbol{\Gamma})\mathrm{d}M\mathrm{d}Z \\
&= \int_{\mathbb{R}^{3N}} d^{3N}\boldsymbol{x} \int_{\mathbb{R}^{3N}} d^{3N}\boldsymbol{v}\,\mathrm{e}^{-\iota\mathcal{L}t} f_{\boldsymbol{\Gamma}}(\boldsymbol{\Gamma}) \qquad (11) \\
&= \int_{\mathbb{R}^2} \mathrm{d}\,\widehat{\Omega} \int_{\mathbb{R}} \mathrm{d}r_{\rm hel}\mathfrak{J}\rho(\boldsymbol{x}; t),
\end{aligned}
$$

where $\mathfrak{J} = r_{\rm hel}^2|\cos b|$ is the Jacobian of the transformation T between the system of galactocentric coordinates $(O, \boldsymbol{x})$ to standard galactic coordinates $(\odot, r_{\rm hel}, l, b)$:

$$
T : \begin{cases} x = \mathrm{R}_\odot - r_{\rm hel}\cos b\cos l \\ y = r_{\rm hel}\cos b\sin l \\ z = \mathrm{z}_\odot + r_{\rm hel}\sin b, \end{cases} \qquad (12)
$$

where $\mathrm{R}_\odot = \sqrt{x_\odot^2 + y_\odot^2}$. After this integral is evaluated, the relative number of stars within a given FOV is obtained as a function of observable quantities (e.g. the galactic coordinates) no matter how large the FOV is (Fig. 2). Although $r_{\rm hel}$ can be unbounded, in practice it is limited by the survey magnitude limits with Pogson's law and the dust extinction by taking into account an extinction model (Section 6.2.1). We point out how the cone-geometry of Fig. 2 for the volume $\int \mathrm{d}\,\widehat{\Omega}\,\mathrm{d}r_{\rm hel}$ is of exemplificative nature. In practice, because every observed star has much larger uncertainty in distance $r_{\rm hel} + \delta r_{\rm hel}$ than in angular position $\{l \pm \delta l, b \pm \delta b\}$, i.e. $|\frac{\delta r_{\rm hel}}{r_{\rm hel}}| \gg |\frac{\delta l}{l}|$ and $|\frac{\delta r_{\rm hel}}{r_{\rm hel}}| \gg |\frac{\delta b}{b}|$, the mapping of the synthetically generated $f_{\rm CSP}^{\rm MW}$ of every survey has a different nature. $\{l, b\}$ are not randomly generated but assumed from the data that we want to analyse without errors while $r_{\rm hel}$ is randomly generated within $r_{\rm hel} \pm \delta r_{\rm hel}$ depending on the particular selection function.
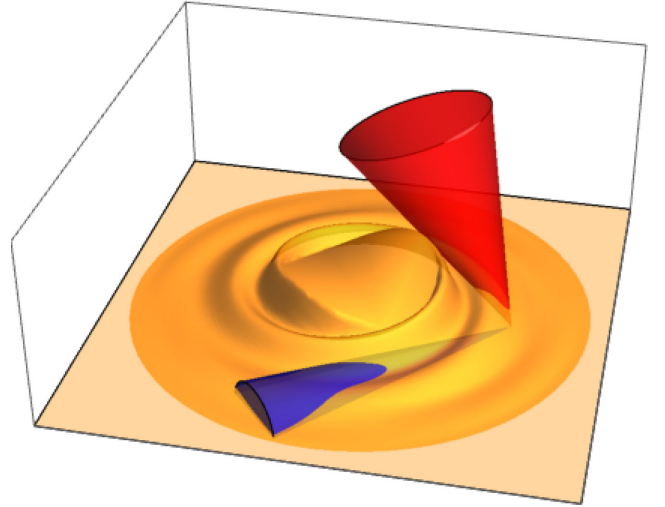

Figure 2. Spiral arm stellar isocontour. The intersection of the yellow surface with the FOV (e.g. violet or red) is the integral performed in equation (11). Two arbitrary solid angles, in blue or red, intersect a single spiral arm SSP over its complicated density profile (orange), from a common solar position slightly outside the plane of the galaxy. The relative contribution to the number of stars in a given l.o.s. is the result of the intersection of the global CSP with the arbitrary cone of the l.o.s.

4 THE AXISYMMETRIC MW: DENSITY DISTRIBUTIONS, GRAVITATIONAL POTENTIALS AND KINEMATICS

In the context of the theory of stellar population introduced above, we can simplify equation (8) and obtain the mass density $\rho(\boldsymbol{x})$ as follows:

$$
\begin{aligned}
\rho &= \int_{\mathbb{R}^{3N}\times\mathbb{R}^2} M f_{\rm CSP}^{\rm MW}\mathrm{d}M\mathrm{d}Z d^{3N}\boldsymbol{v} \\
&= \int_{\mathbb{R}^{3N}} \mathrm{e}^{-\iota\mathcal{L}t} f_{\boldsymbol{\Gamma}}(\boldsymbol{\Gamma}; t_0)\, d^{3N}\boldsymbol{v} \qquad (13) \\
&\simeq \int_{\mathbb{R}^3} \mathrm{e}^{-\iota\mathcal{B}t} f_{\boldsymbol{\gamma}}(\boldsymbol{\gamma}; t_0)\, d^3\boldsymbol{v},
\end{aligned}
$$

where in the last row of the equation we reduced the dimensionality of the phase-space by remembering that it is possible to show that the two-body relaxation time t_{2b} (considered in the approximation of independent-hyperbolic encounters) is long enough to allow us to treat the Galaxy to a good approximation as a 'collisionless' system. Hence we can substitute the discrete stellar distribution with a continuous density profile, and the Liouville operator $\mathcal{L}$ can be substituted with the more simple Boltzmann operator $\mathcal{B}[f_{\boldsymbol{\gamma}}] \equiv \iota\{H, f_{\boldsymbol{\gamma}}\}$, with H one-particle Hamiltonian and $\{*, *\}$ the Poisson brackets (ι is the imaginary unit).

Unfortunately, the explicit form of $f_{\rm CSP}^{\rm MW}$ is unknown (the blue manifold in Fig. 1) or has to be inferred just from simple theoretical considerations. For this reason, we decided to base our modelling technique on the density distributions of stars and dark matter (DM). From the density profiles, the potential and hence the kinematics is computed. Furthermore, from the same density profiles the relative number of stars per bin of colour and magnitude along an l.o.s. in the CMD is computed. This approach is not the only possible way to proceed in analytical modelling, but we are guided by the explicit intention to present a model focused on the interpretation of the data, where the data are the protagonist in leading our understanding of the phenomenon 'Galaxy'.

Therefore, it is of paramount importance to assign to each component of the MW a plausible density profile $\rho(\boldsymbol{x})$ to derive a correct global gravitational potential. In the following, we present our treatment of the Poisson equation and hence the global gravitational potential of the MW. These results will represent the axisymmetric foundations of our description the DWT of spiral arms. The gravitational potential is derived for all components of the MW even if we will focus only on the disc components for which, thanks to their proximity, data of good quality can be acquired and accurate descriptions are possible.

In our model, the location of the Sun is assumed to be at $\boldsymbol{x}_\odot = \{R_\odot, \phi_\odot, z_\odot\} = \{8.00, 0.00, 0.02\}$ kpc in a reference frame centred on the (yet unknown) mass barycentre of the axisymmetric model of the MW we are going to build up.

4.1 Axisymmetric SSP models

4.1.1 Thin and thick disc

As mentioned above in equation (4), we consider a multicomponent model of stellar populations. For the ith component of the thin or thick disc, we implemented a double exponential form of the density profiles, that is, with an exponential profile decreasing with Galactocentric radius and vertical distance from the plane. Alternative vertical profiles (power law and secant-square) are available for investigation but not breaks of the exponential profiles has been implemented (e.g. Pohlen & Trujillo 2006). Because we are going to develop a kinematics model, no time dependence of the density profiles is assumed. Written in cylindrical coordinates to exploit the ϕ-symmetry the profile reads

$$\rho_D(R, \phi, z) = \rho_\odot e^{-\frac{R-R_\odot}{h_R} - \frac{z-z_\odot}{h_z}}. \tag{14}$$

This parametric formalism depends on the density at the solar neighbourhood $\rho_\odot$ and two scale parameters: scalelength h_R and scaleheight h_z for each stellar population considered. It does not contain an explicit dependence on ϕ. The potential is conveniently expressed as function of one single integral with integrand depending on the Bessel function (e.g. Bienayme, Robin & Creze 1987) being hence extremely rapid to compute:

$$\Phi_D(R, \phi, z) = -4\pi G \rho_0 h_R^{-1} \int_0^\infty J_0(kR)(h_R^{-2} + k^2)^{-3/2}$$

$$\times \frac{h_z^{-1} e^{-k|z|} - k e^{-h_z^{-1}|z|}}{h_z^{-2} - k^2} dk, \tag{15}$$

where J_0 is the Bessel function of the first kind (e.g. Abramowitz & Stegun 1972) and the scale parameter for each component ith should be taken into account but omitted for the sake of simplicity.

The kinematic description of these disc populations is in principle obtainable self-consistently from the numerical solution of systems as equation (22) in Cuddeford & Amendt (1992). However, aside from the numerical difficulties, this description would require difficult observational validation (e.g. by requiring second-order derivatives) that makes it challenging to apply for precise surveys such as the forthcoming *Gaia*. For this reason, we have chosen in favour of an approach based on the Jeans equations. Following Pasetto et al. (2012c,d), we are not assuming a shape for the $f_\gamma(\gamma; t)$ but working on the methods-of-moments of the collisionless Boltzmann equation in agreement with the simplification of equation (13). The mean circular velocity and asymmetric drift

can then be studied with the relation:

$$\bar{v}_\phi(R, z) = \begin{pmatrix} |\bar{v}_\phi| \dfrac{r_{\rm hel} \cos b \cos l}{R} \\ |\bar{v}_\phi| \dfrac{R_\odot - r_{\rm hel} \cos b \cos l}{R} \\ 0 \end{pmatrix},$$

$$|\bar{v}_\phi| = \left(v_c^2 - \frac{\partial \ln \rho_D}{\partial \ln R} \left(\sigma_{RR}^2 + \sigma_{Rz}^2 \right) + \left(\sigma_{RR}^2 + \sigma_{\phi\phi}^2 \right) \right. \tag{16}$$

$$\left. + R \left(\frac{\partial \sigma_{RR}^2}{\partial R} + \frac{\partial \sigma_{Rz}^2}{\partial z} + \frac{\partial \Phi_{\rm tot}(R, z)}{\partial R} \right) \right)^{1/2},$$

where the dependence of the three non-null diagonal terms $\{\sigma_{RR}, \sigma_{\phi\phi}, \sigma_{zz}\}$ on the configuration space will be written in cylindrical coordinates as

$$\sigma_{ii,j}(R, z) = \nabla_z \sigma_{ii,j}(R, z) \left(|z| - z_{j-1} \right) + \sigma_{ii,j-1} \left(R, z_{j-1} \right), \tag{17}$$

for $i = \{R, \phi\}$ and $j = I, II, III$, while the vertical profiles of the thin disc stellar population and the non-diagonal term σ_{Rz} will be introduced in Section 7 and where the underlying assumption of $\frac{\sigma_{RR}^2}{\sigma_{zz}^2} = $ const. is assumed in agreement with the DWT for spiral arms introduced below. On the plane, equation (17) will be forced to match the profiles

$$\begin{cases} \sigma_{RR}^2(R, 0) = \sigma_{RR,\odot} e^{-\frac{R-R_\odot}{h_R}} \\ \sigma_{\phi\phi}^2(R, 0) = \sigma_{zz,\odot} e^{-\frac{R-R_\odot}{h_R}} \\ \sigma_{zz}^2(R, 0) = \left(1 + \frac{\partial \ln v_c}{\partial R} \right) \frac{\sigma_{RR}^2(R,0)}{2}, \end{cases} \tag{18}$$

and the gradients for the three vertical profiles I, II, III are a smooth interpolation of the values in Table 1. Moments of order up to four (obtained directly from cumulants) are evaluated as in appendix of Pasetto et al. (2012c).

4.1.2 Stellar halo

For the ith stellar halo component of the MW, we follow the model proposed in Robin et al. (2003) because it is fine-tuned on the observational constraints, i.e. it is simple in its form but phenomenologically justified. In the original form Robin's profile reads

$$\rho_{H*}(r) = \frac{\rho_{0,H*}}{r_\odot} \begin{cases} r^\alpha & r > h_{rH*} \\ h_{rH*}^\alpha & r \leqslant h_{rH*}, \end{cases} \tag{19}$$

where $\rho_{0,H*}$ is the central stellar halo density, and $h_{rH\star}$ the scalelength parameter. Because we are interested in the potential formalism of this density model, we compute its corresponding potential solving Poisson's equation in spherical coordinates and guaranteeing continuity (but not differentiability) to the formulation as follows:

$$\Phi_{H*}(r) = \begin{cases} 4\pi G \rho_{0,H*} \dfrac{r_\odot^{-\alpha}}{r} \dfrac{(\alpha+2) h_{r,H*}^{\alpha+3} + r^{\alpha+3}}{(\alpha+2)(\alpha+3)} & \wedge r > h_{r,H*} \\ -2\pi G \rho_{0,H*} \dfrac{3 h_{r,H*}^2 - r^2}{3} \left(\dfrac{h_{r,H*}}{r_\odot} \right)^\alpha & \wedge r \leqslant h_{r,H*}, \end{cases} \tag{20}$$

where the scale parameters dependence of the ith-component of stellar halo is omitted.

For the kinematics description of the stellar halo several models for $f_{\rm SSP}^{H*}$ are available in the literature with different flavours of parameters (multiscale parameters, anisotropy, etc.). Nevertheless,

Table 2. Kinematic and dynamical properties of the MW components. The first two thin disc stellar components implement the spiral arm treatment described in the text. Because a map of the metallicity gradients $\nabla_x [\frac{Fe}{H}]$ is still uncertain, no standard default values are assumed and they are used as free parameters. Standard star formation profiles are adopted (e.g. Chiosi 1980, Fig. 3).

Components	Scale parameters	Δt (Gyr)	$[\frac{Fe}{H}]$ (dex)	$\sigma_{ii\odot}$ (km s^{-1})
	$\{\rho_D, h_R, h_z\}_\odot$ [M$_\odot$ kpc^{-3}, kpc, kpc]			
Thin disc pop 1 (sp)	1.29×10^7, 2.57, 0.06	[0.1, 0.5]	[−0.70, 0.05]	27.0,15.0,10.0
Thin disc pop 2 (sp)	1.93×10^7, 2.59, 0.06	[0.5, 0.9]	[−0.70, 0.05]	30.0,19.0,13.0
Thin disc pop 3	4.96×10^7, 2.96, 0.07	[0.9, 3.0]	[−0.70, 0.05]	41.0,24.0,22.0
Thin disc pop 4	3.38×10^7, 2.99, 0.09	[3.0, 7.5]	[−0.70, 0.05]	48.0,25.0,22.0
Thin disc pop 5	3.34×10^7, 3.41, 0.25	[7.5, 10.0]	[−0.70, 0.05]	52.0,32.0,23.0
Thick disc	2.40×10^6, 2.23, 1.35	[10.0,12.0]	[−1.90,−0.60]	51.0,36.0,30.0
ISM	2.26×10^7, 4.51, 0.20			
	$\{\rho_{0,H*}, d_{0,H*}, h_{r H*}, \alpha\}$ [M$_\odot$ kpc^{-3}, kpc, kpc]			
Stellar halo pop 1	2.18×10^4, 1.00, 1.00, −2.44	[12.0,13.0]	< -1.90	151.0,116.0,95.0
	$\{M_B, h_{r, B}\}$ [M$_\odot$, kpc]			
Bulge pop 1	3.4×10^{10}, 0.7	[6.0,12.0]	[−0.40,+0.30]	
	$\{v_0, h_{r, DM}, q\}$ [km s^{-1}, kpc]			
DM	139.04, 6.70, 0.89			

self-consistent models rely on a description of the halo as a dynamically relaxed population. This is clearly a non-physical assumption for a stellar population as the halo which is composed by old stars but dynamically young, non-phase-mixed, rich in substructures as stellar streams (see e.g. Belokurov et al. 2006).

4.1.3 DM and hot-coronal gas

The only component that we can start from the potential shape is the DM component, because its presence is indirectly manifest but it is not directly observed. We select a simple balance between gravity and centrifugal forces for circular orbits to obtain the logarithmic potential:

$$\Phi_{DM}(R, \phi, z) \equiv \frac{v_{0,DM}^2}{2} \log \left(h_{R,DM}^2 + R^2 + q^{-2}z^2 \right), \tag{21}$$

where v_0 is the scale velocity, $h_{R,DM}$ the scalelength and q the flattening factor. The density profile can again be obtained by use of Poisson's equation as

$$\rho_{DM} = \frac{v_0^2}{4\pi G} \frac{q^2 \left(h_{r,DM}^2 (2q^2 + 1) + R^2 + 2z^2 \right) - z^2}{\left(q^2 \left(h_{r,DM}^2 + R^2 \right) + z^2 \right)^2}. \tag{22}$$

No compelling reasons exist so far to split DM in more components and the model does not consider substructures of the DM component (e.g. Yoon, Johnston & Hogg 2011). We expect not to detect granularity in the DM distribution from the kinematic anomalies of the closest stars kinematics. In view of this, the presence of granularity in the DM distribution, mimicking DM streams, are neglected in our model.

We complete the review by mentioning that optionally we can include axisymmetric components adding a hot coronal gas. This does not influence the closest stellar dynamics of the MW stars but in mass it is thought to contribute up to $\sim 5 \times 10^{10}$ M$_\odot$ within ~ 200 kpc from the MW galaxy centre (see e.g. Pasetto et al. 2012a, and reference therein for a model including it).

4.1.4 Bulge

A separate work is in preparation on the kinematical treatment of the central part of the Galaxy which is of course very important. Unfortunately, up to now the modelling of the bulge is still imprecise and a subject of debate. A recent finding of Dékány et al. (2015) shows an example of the ongoing research and constantly changing knowledge that we have about the central regions of the MW. Nevertheless, in the total potential a bulge component has to be accounted for and we adopt the following spherical density-potential 'couple' (Hernquist 1990) from which kinematics is implemented too:

$$\begin{cases} \rho_B(r) = \frac{M_B h_{r,B}}{2\pi r(r+h_{r,B})^3} \\ \Phi_B(r) = -\frac{GM_B}{r+h_{r,B}}, \end{cases} \tag{23}$$

where again the dependence of the scale parameters $\{M_B, h_{r, B}\}$, bulge mass and scale radius, respectively, from the stellar bulge component is understood even though the subscript is omitted.

This series of equations represent the basic potential in axisymmetric approximation. The chosen density parameters that we are going to assume for these profiles are presented in Table 2 as results of the technology that we are going to introduce in Section 5.

These parameters are chosen in such a way that they nicely reproduce some important observational constraints (see also appendix A of Pasetto 2005 and Pasetto et al. 2012c).

4.2 Axisymmetric SSP constraints

4.2.1 Circular velocity

To date several studies have covered the most important dynamical constraints on the MW potential, i.e. its rotation curve, from several data sets and with different techniques, both for the total stellar rotation, for gas rotation or for single MW stellar populations (e.g. Levine, Heiles & Blitz 2008; Xue et al. 2008; Deason, Belokurov & Evans 2011; Deason et al. 2012; Fermani & Schönrich 2013;
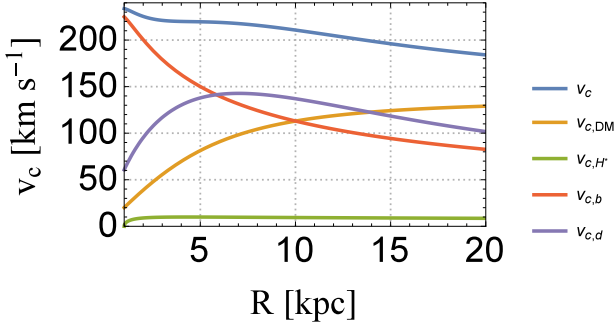
Figure 3. Circular velocities as a function of the radius and contribution from each stellar component of the model of the galaxy. See the text for the definitions of the equation for the rotation curve of each subpopulation.

Xin & Zheng 2013; Bhattacharjee, Chaudhury & Kundu 2014; López-Corredoira 2014, to quote a few). From the potential adopted here, we obtained the rotation curve analytically as $v_c = \sqrt{r \frac{\partial \Phi}{\partial r}}$, where the individual components are not difficult to evaluate. Using equation (21), we get for the DM component:

$$v_{c,\mathrm{DM}}^2 = \frac{R^2 v_0^2}{R^2 + h_{r,\mathrm{DM}}^2}; \tag{24}$$

from equation (20) for the stellar halo profile we have

$$v_{c,H^*}^2 = \begin{cases} \frac{4\pi G}{r^2(\alpha+3)} \frac{r}{r_\odot^\alpha} \sum_{H^*} \rho_{0,H^*} \left(r^{\alpha+3} - h_{r,H^*}^{\alpha+3}\right) & h_{r,H^*} < r \\ \frac{4\pi G}{3} \frac{r}{r_\odot^\alpha} \sum_{H^*} \rho_{0,H^*} h_{r,H^*}^\alpha & r < h_{r,H^*}, \end{cases} \tag{25}$$

where we assumed the same $\alpha \forall H^*$, $H^* \in \mathbb{N}$ indexing the stellar populations, i.e. with a simple abuse of notation we wrote $v_{c,H^*}^2 = \sum_{H^*=1}^{N_{H^*}} v_{c,H^*}^2$ with N_{H^*} number of stellar halo populations implemented in Table 2 (one in this case). For the bulge population from equation (23), we get

$$v_{c,B}^2 = GR \sum_B \frac{M_B}{(R + h_{r,B})^2}, \tag{26}$$

with $B \in \mathbb{N}$ indexing the populations as above. The disc components are only slightly more complicated by the presence of the Bessel function that can be nevertheless handled numerically (e.g. Abramowitz & Stegun 1972) from equation (15) in the form:

$$v_{c,D}^2 = 4\pi GR \sum_D \rho_{0,D} \int_0^\infty \mathrm{d}k \frac{1}{h_{R,D} \left(h_{R,D}^{-2} + k^2\right)^{3/2}} \frac{k J_1(kR)}{h_{z,D}^{-1} + k}, \tag{27}$$

where $D \in \mathbb{N}$ indexes the disc populations.

Finally in Fig. 3, we present the velocity curves of the various components of the Galaxy according to the corresponding density profiles already discussed above and with parameters summarized in Table 2 as a result of the technique presented in Section 5.

4.2.2 Oort functions: $O^\pm$

The slope of the rotation curve, locally related to the Oort's constants, has long been known to depend on the local gas content, which does not monotonically vary with the radius and contributes significantly to the local gradient of the rotation curve (Olling & Merrifield 1998; Olling & Dehnen 2003; Minchev & Quillen 2007). The profile of these functions outside the solar neighbourhood is what we refer to as 'Oort functions'. We will present in the next section a map distribution of the gas content in relation to dust

distribution and extinction (Fig. 8). In the future, the estimation of the Oort function will represent a challenge for large kinematic surveys such as *Gaia*. The Oort functions are defined as $O^\pm(R) \equiv \pm \frac{1}{2} (\frac{v_c}{R} \mp \frac{\mathrm{d}v_c}{\mathrm{d}R})$. Perhaps the greatest difficulty in estimating the Oort functions derives from the presence of the derivatives in their definition. Unfortunately, current observations of the rotational motion of the MW are not good enough to allow a calculation of the derivatives in $O^\pm(R)$ directly from the data (Kerr & Lynden-Bell 1986; Hanson 1987). It is also possible to determine $O^+ - O^- = \frac{v_c}{R}$ in an independent way from the individual values of O^+ and O^- from proper motion surveys in the direction $l = 90°$ or $l = 270°$. Because along these directions the stars have a small dependence on the Galactocentric radius so the estimations are less affected by the radial dependence of the Oort functions. Finally, the combination $-\frac{O^-}{O^+ - O^-}$ can be estimated from the velocity ellipsoid of random stellar motions. For the first function $O^+ \equiv O^+(R)$, a compact formulation can be obtained as follows. For the DM component,

$$O_{\mathrm{DM}}^+(R) = \frac{1}{4v_c} \frac{2R^3 v_0^2}{\left(R^2 + h_{r,\mathrm{DM}}^2\right)^2}, \tag{28}$$

for the stellar halo components of Robin's density profiles

$$O_{H^*}^+(R) = -\frac{\pi G}{v_c} \frac{r_\odot^{-\alpha}}{(\alpha+3) r^2} \sum_{H^*} \rho_{0,H^*} \left(\alpha r^{\alpha+3} + 3 h_{r,H^*}^{\alpha+3}\right), \tag{29}$$

for $h_{r,H^*} < r$, while it is clearly null inside the scale radius. For the bulge components' contribution, we can write

$$O_B^+(R) = \frac{G M_B}{4v_c} \sum_B \frac{3R + h_{r,B}}{(R + h_{r,B})^3}, \tag{30}$$

and finally for the stellar discs contribution we can write

$$O_D^+(R) = \frac{\pi G R}{v_c} \sum_D \frac{\rho_{0,D}}{h_{R,D}} \int_{\mathbb{R}} \mathrm{d}k \frac{k^2 J_2(kR)}{h_{z,D}^{-1} + k} \frac{1}{\left(h_{R,D}^{-2} + k^2\right)^{3/2}}. \tag{31}$$

Analogously for the O^- function, we can write for the DM component

$$O_{\mathrm{DM}}^-(R) = \frac{v_0^2}{2v_c} \frac{R^3 + 2R h_{r,\mathrm{DM}}^2}{\left(R^2 + h_{r,\mathrm{DM}}^2\right)^2}, \tag{32}$$

for the stellar halo it reads

$$O_{H^*}^-(R) = \frac{\pi G}{v_c} \frac{r_\odot^{-\alpha}}{(\alpha+3) r^2} \sum_{H^*} \rho_{0,H^*} \left((\alpha+4) r^{\alpha+3} - h_{r,H^*}^{\alpha+3}\right). \tag{33}$$

Differently from O^+, the contribution from the stellar halo in the central zones for Robin's profile is not null, but

$$O_{H^*}^-(R) = \frac{16\pi Gr}{3} \sum_{H^*} \rho_{0,H^*} \left(\frac{h_{r,H^*}}{r_\odot}\right)^\alpha, \tag{34}$$

for $r \leqslant h_{r,H^*}$. The level of this contribution is nevertheless extremely weak and added here only for completeness. Effectively, it is null compared with the dominant contribution of the bulge component:

$$O_B^-(R) = \frac{1}{4v_c} \sum_B G M_B \frac{R + 3h_{r,B}}{(R + h_{r,B})^3}. \tag{35}$$

Finally, the most significant contributions that account for star and the local gas distributions are given by

$$O_D^-(R) = 4\pi G \sum_D \frac{\rho_{0,D}}{h_{R,D}} \int_{\mathbb{R}} \mathrm{d}k \frac{k}{h_{z,D}^{-1} + k} \frac{k R J_0(kR) + 2 J_1(kR)}{\left(h_{R,D}^{-2} + k^2\right)^{3/2}}. \tag{36}$$

With this equation and the parameters of Table 1, we obtain the following values at the solar position: $O^+ = 15.1 \, \text{km s}^{-1} \, \text{kpc}^{-1}$ and $O^- = -13.1 \, \text{km s}^{-1} \, \text{kpc}^{-1}$. For comparison, the study of *Hipparcos* proper motions by Feast & Whitelock (1997a,b) yield $O^+(\text{R}_\odot) = 14.8 \pm 0.8 \, \text{km s}^{-1} \, \text{kpc}^{-1}$ and $O^+(\text{R}_\odot) - O^-(\text{R}_\odot) = 27.2 \pm 0.9 \, \text{km s}^{-1} \, \text{kpc}^{-1}$ and by Dehnen & Binney (1998) yield $O^+(\text{R}_\odot) = 14.5 \pm 1.5 \, \text{km s}^{-1} \, \text{kpc}^{-1}$ and $O^+(\text{R}_\odot) - O^-(\text{R}_\odot) = 27.20 \pm 1.5 \, \text{km s}^{-1} \, \text{kpc}^{-1}$.

4.2.3 Vertical force

The last significant constraint that we consider in the determination of the MW potential is the force acting vertically on the plane. This constraint is of paramount importance to tune the vertical profiles of the disc and the vertical epicyclic oscillations of the orbits, thus several studies have investigated the vertical structure of the MW on the basis of different observations (Haywood, Robin & Creze 1997; Chen et al. 2001; Soubiran, Bienaymé & Siebert 2003; Levine et al. 2008; Bovy et al. 2012b; Jałocha et al. 2014). We determine the vertical force at any location within the galaxy as follows.

For the DM component, we evaluate the vertical gradient of the potential at any radial and vertical location as

$$F_{z,\text{DM}} = \frac{v_0^2 z}{q^2 \left(R^2 + h_{r,\text{DM}}^2\right) + z^2},\qquad(37)$$

that retains information of the flattening parameter q of the DM halo. Unfortunately, the alignment of the DM halo component with the principal axis of symmetry of the gravitational potential is far from clear. The triaxiality and the directions of the eigenvectors of the inertia tensor of the DM mass distribution is at present unknown and the problem of the stability of rotating discs inside triaxial haloes is weakly understood from the theoretical point of view and still a matter of debate (e.g. Debattista et al. 2013, and reference therein). We will take q into account only for completeness and eventually add a flattening of the DM profiles while moving inward in the Galaxy. For the stellar halo components, the same computation yields

$$F_{z,H*}(R,z) = \frac{4\pi G z r_\odot^{-\alpha}}{\alpha + 3} \sum_{H*} \rho_{0,H*} \left(r^\alpha - \frac{h_{r,H*}^{\alpha+3}}{r^3}\right),\qquad(38)$$

for $\sqrt{R^2 + z^2} = r > h_{r,H*}$, and

$$F_{z,H*}(R,z) = 4\pi G \sum_{H*} \frac{\rho_{0,H*} z}{3} r_\odot^{-\alpha} h_{r,H*}^\alpha,\qquad(39)$$

otherwise. Analogously for the bulge components, we get

$$F_{z,B}(R,z) = \frac{z}{\sqrt{R^2 + z^2}} \sum_B \frac{G M_B}{\left(\sqrt{R^2 + z^2} + h_{r,B}\right)^2}.\qquad(40)$$

Finally, for the disc component we get

$$F_{z,D}(R,z) = 4\pi G \sum_D \frac{\rho_{0,D}}{h_{R,D} h_{z,D}}$$

$$\times \int_{\mathbb{R}} dk \, \frac{e^{k|z|} - e^{h_{z,D}^{-1}|z|}}{k^2 - h_{z,D}^{-2}} \frac{k J_0(kR) e^{-|z|\left(h_{z,D}^{-1} + k\right)}}{\left(h_{R,D}^{-2} + k^2\right)^{3/2}}.\qquad(41)$$

Our MW potential model with the values of Table 2 presents a value of $\frac{|F_z(1.1\text{kpc})|}{2\pi G} = 70.0$ for the total vertical force on the plane that match exactly the standard literature values of Kuijken & Gilmore (1989b, see also Kuijken & Gilmore 1989a,c) and $\frac{|F_z(2.0\text{kpc})|}{2\pi G} = 87.9$

at the solar potion $\text{R}_\odot = 8.0$ and $\phi_\odot = 0.0$ (e.g. see Bienaymé et al. 2014, for compatible values at $\text{R}_\odot = 8.5$). We consider these as the major contributors to the shape of the underlying MW potential. Adding other constraints will not significantly change the distribution of the stars in the CMDs and their kinematics.

4.2.4 Further constraints

By integrating the density profiles of equations (14), (19), (22) and (23), we obtain the total mass as a direct sum of the mass of the components. For the DM this integration reads

$$M_{\text{DM}} = \frac{v_0^2}{G} \frac{r_{\text{max}}^3}{r_{\text{max}}^2 + h_{r,\text{DM}}^2},\qquad(42)$$

for the stellar halo components

$$M_{H*} = \frac{4\pi r_\odot^{-\alpha}}{3(\alpha+3)} \sum_{H*} \frac{\rho_{0,H*}}{d_{0,H*}} \left(3 r_{\text{max}}^{\alpha+3} + \alpha h_{r,H*}^{\alpha+3}\right),\qquad(43)$$

for the bulge

$$M_B = 4\pi G r_{\text{max}}^2 \sum_B \frac{M_B}{\left(h_{r,B} + r_{\text{max}}\right)^2},\qquad(44)$$

and for the discs, by proceeding arbitrarily with an integration in cylindrical coordinates, we can write

$$M_D = 4\pi \sum_D \frac{\rho_{0,D} e^{-R_{\text{max}} h_{R,D}^{-1}}}{h_{R,D}^{-2} h_{z,D}^{-1}} \left(e^{R_{\text{max}} h_{R,D}^{-1}} - R_{\text{max}} h_{R,D}^{-1} - 1\right).\qquad(45)$$

With the parameters in Table 1, we obtain a total mass of $M = 1.12 \times 10^{12} \, \text{M}_\odot$ for $r_{\text{max}} = 100$ kpc (e.g. Olling & Merrifield 2001; Gerhard 2002; Klypin, Zhao & Somerville 2002; Widrow, Pym & Dubinski 2008; Xue et al. 2008; McMillan 2011; Bhattacharjee et al. 2014; Bratek et al. 2014; Kafle et al. 2014; Licquia & Newman 2015; Huang et al. 2016). This constraint has several implications on the orbits of the dwarf galaxy satellites of the MW, and several studies have focused on total mass determination and on the escape speed from the MW (e.g. Dehnen & Binney 1998; Wilkinson & Evans 1999; Smith et al. 2007; Xue et al. 2008; McMillan 2011; Licquia & Newman 2013; Bhattacharjee et al. 2014).

Finally, the determination of the local surface mass density is tightly related to the integration presented for the total mass. This is computed in our modelling only for the disc components $\Sigma_D = 2 \sum_D \frac{\rho_{c,D}}{h_{z,D}^{-1}} e^{-R h_{R,D}^{-1}}$. This is a relevant constraint especially in relation to the disc modelling of the spiral arms that we are going to present here. With the parameters of Table 1, we estimate a value of $\Sigma_D = 41 \, \text{M}_\odot \text{pc}^{-2}$ at $R = \text{R}_\odot$.

We do not consider here a few other issues of minor importance that a standard axisymmetric model should take into account such as, e.g. the terminal velocities for the inner Galaxy (Vallenari et al. 2006). Although it may provide a better constraint than Oort's constants for an axisymmetric galaxy, it severely affected by noncircular motions of the ISM. Its interpretation needs much more precise mapping of the galactic gas distribution (see also Golubov & Just 2013; Chemin, Renaud & Soubiran 2015). In this respect, Section 6.2.1 we will present our new non-axisymmetric distribution of gas.

5 MACHINE LEARNING

To obtain values representative of the MW stellar, gas and DM components (Table 2) we tune the free parameters of the

density-potential couples formulated in the previous section on theoretical and observational constraints. The choice to represent a given set of data with a fixed number n of SSP is one of the major underlying constraints that we have adopted in our formalism. This forced us to a statistical interpretation of *parametric*-nature and hence a *supervised*-machine learning approach. Unsupervised learning in the framework of neural networks will be explored in a future investigation (Pasetto 2016, in preparation).

Within this parametric approach, among the most sophisticate and robust techniques available to date are the genetic algorithms. A genetic algorithm is an adaptive stochastic optimization algorithm involving search and optimization, and it was first introduced by Holland (1975). Holland created an electronic organism as a binary string ('chromosome'), and then used the genetic and evolutionary principles of fitness-proportionate selection for reproduction, random crossover, and mutation to explore the space of solutions. The so-called 'genetic programming languages' apply the same principles using an expression tree instead of a bit string as a 'chromosome'. In astronomy, the Pikaia genetic algorithm has been already considered in the galactic kinematics in (see 2005 Pasetto, PhD thesis, Charbonneau 1995; Metcalfe & Charbonneau 2003). We consider the following quite generic task to model a given data set with a set of adjustable parameters. This task consists of finding the single parameter set that minimizes the difference between the model's predictions and the data. A 'top-level' view of the canonical genetic algorithm for this task can be read as follows: we start by generating a set ('population') of trial solutions, usually by choosing random values for all model parameters; then evaluate the goodness of fit ('fitness') of each member of the current population (e.g. through a chi-square measure with the data). Then the algorithm selects pairs of solutions ('parents') from the current populations, with the probability of a given solution being selected made proportional to that solution's fitness. It breeds the two solutions selected and produces two new solutions ('off-spring'). It repeats the selection of the population and its progeny until the number of off-springs equals the number of individuals in the current population by replacing the new population of off-springs over the old one. It then repeats the whole sequence until some termination criterion is satisfied (i.e. the best solution of the current population reaches a fit goodness exceeding some preset value).

A genetic-algorithm based approach to a given optimization task, as defined above, resembles a kind of forward-modelling: no derivatives of the fit function goodness with respect to model parameters is needed to be computed. Nothing in the procedure outlined above depends critically on using a least-squares statistical estimator; any other robust estimator could be used, with little or no change to the overall procedure. In the kinematical applications, the model needs to be evaluated (i.e. given a parameter set, compute a synthetic data set and the associated goodness of fit).

In the process of CMD fitting, the genetic algorithm has a long history in the Padua group starting from the works of Ng et al. (2002) and has been implemented in the kinematic fitting of observational data in Vallenari et al. (2006). The algorithm has been run on true data to reproduce radial velocities (Gilmore, Wyse & Norris 2002), the GSC-II proper motion catalogue Vallenari et al. (2006) and the RAVE data set equipped with 2MASS proper motions in Pasetto et al. (2012d, 2012c). The detailed study of the MW potential is beyond the goal of this paper (and maybe meaningless at the sunrise of the *Gaia*-era), but we limit ourselves to present in Table 1 the guest parameters for the MW potential just introduced and achieved so far. They will represent the starting values of the founding potential that we are going to perturb in the next section

to obtain the spiral arms description which represents the core of this work.

6 DENSITY DESCRIPTION OF NON-AXISYMMETRIC FEATURES

The axisymmetric potential that we have introduced above and summarized in equation (2) represents the starting point for the perturbative approach that we introduce hereafter.

As previously anticipated, the first framework that we are introducing is the DWT. It deals in its original form with the description of the in-plane motion of the stars in a spiral galaxy. It is a linear response theory for an unperturbed generalized Schwarzschild distribution function (SDF):

$$Q \equiv (\boldsymbol{v} - \bar{\boldsymbol{v}})^T \boldsymbol{\sigma}_v^{-1}(\boldsymbol{x}; t)(\boldsymbol{v} - \bar{\boldsymbol{v}}),$$
$$f^{\text{Sch}} \equiv e^{-1/2 Q(\boldsymbol{x}) + \eta}, \tag{46}$$

where Q is a quadratic positive definite form, $\boldsymbol{\sigma}_v(\boldsymbol{x}; t)$ a second rank symmetric tensor defined in equation (9), $\eta(\boldsymbol{x})$ a continuous and differentiable scalar function and with the superscript $(*)^T$, we refer to the transpose of an array and with $(*)^{-1}$ to the inverse element of an array (not the inverse matrix). It is normalized accordingly with $(2\pi)^{-3/2} |\boldsymbol{\sigma}|^{-1/2} e^{-\eta/2} \equiv (2\pi)^{-3/2} |\boldsymbol{\sigma}|^{-1/2} \Sigma_0(R)$. We will recall in what follows the basis of this theoretical framework of the DWT without explicit proof, but we will present a new hypergeometric form for the expression of the first moments of the perturbed DF that were previously known only in an integral form. We will highlight the advantages of our formulation.

The second perturbative framework adopted here has been developed by Amendt & Cuddeford (1991) and it has been previously adopted in our modelling technique by Pasetto, PhD thesis 2005 in Vallenari et al. (2006). Here, we will only recall the theoretical basis of this second perturbative framework dealing with the vertical behaviour of the kinematics above and below the disc plane, and we will compare it with the DWT. In the axisymmetric case, the matrix $\boldsymbol{\sigma}_v(\boldsymbol{x}; t)$ acquires an especially simple diagonal form and the dependence of the three non-null diagonal terms has been already introduced in Section 4.1.1.

6.1 Linear response theory to a spiral perturbation pattern

The most popular self-consistent fully analytical treatment available in literature to study the spiral arms is based so far on the DWT proposed by Lin et al. (1969) and Marochnik & Suchkov (1969a,b). In these works, a sinusoidal perturbation to the axisymmetric potential for a discoidal stellar distribution is considered. This description stands on two theoretical pillars of the stellar dynamics: the epicycles approximation theory and linear response theory to Boltzmann collisionless equation (see also Section 2). Here, we limit ourselves to introduce the basic functions as definitions, without proofs, forwarding the reader to specialized text on stellar dynamics for a coherent exposition of these topics (e.g. Bertin 2014). If we perturb an axisymmetric potential with a sinusoidal wave, we need to search for the self-consistent condition for a potential of a spiral drawn by a shape-function $\psi(R) \equiv -2 \cot(p) \log(\frac{R}{R_0})$ where p is the pitch angle $p \sim 8°$, R_0 is the starting radius of the spiral perturbation, $R_0 \sim 2.6 \text{ kpc}$, and $m = 2$ is the number of spiral arms that we assume. The values adopted here are examples for the MW case but they have not been deduced through data analysis of Section 5. A large literature review has been presented in Section 1.1 from where we extracted the adapted values for the exercise presented below. The

variable Ω_p is the rotation pattern of the spiral structure; the theory so far is developed for a constant Ω_p, even though no strong observational constraints are available to justify this assumption. Recent N-body simulation studies suggest $\Omega_p = \Omega_c(R)$, where $\Omega_c(R)$ is the angular speed at R (e.g. Wada, Baba & Saitoh 2011; Grand, Kawata & Cropper 2012a), while the other studies interpret the spiral arms in N-body simulations as overlapping multiple-density waves covering different radial ranges, with different pattern speed, $\sum_i \Omega_{p,i}$. and slower pattern speeds in the outer region (Roškar et al. 2012; Sellwood & Carlberg 2014). Nevertheless, no strong observational evidence is available to date to formalize $\Omega_p = \Omega_p(R, \phi, z; t)$.

In what follows, we will simply assume $\Omega_p \sim 35.0\,\mathrm{km\,s^{-1}\,kpc^{-1}}$. We define $\Phi^a(R) \equiv -\Phi_0^a R\,\mathrm{e}^{-R/h_s}$ to be amplitude of the spiral arm potential profile, where an indicative scalelength $h_s \sim 2.5$ kpc is assumed and $\Phi_0^a \sim 887.0\,\mathrm{km^2\,s^{-2}\,kpc^{-1}}$ from Roca-Fàbrega et al. (2014). These numerical values are taken from the literature reviewed in Section 1.1 and are of illustrative nature to the present capability of our modelling approach alone. They are not meant to be best-fitting values through the technology explained in Section 5 to any particular survey.

The DWT is developed in epicycle approximation. The epicycle approximation is probably the weakest of the assumptions adopted in our model. In the next section, we will review some observational evidence of the failure of this approximation in the solar neighbourhood. Here, we proceed simply by adopting the modification that the perturbative linear approach induces on this approximation, without presenting a critical review, even though improved tools are already available (Dehnen 1999a). The main role of this approximation is to decouple in equation (46), the radial/azimuthal from the vertical direction thus simplifying them. From the potential introduced in the previous sections, we can define the rotation frequency as $\Omega(R) \equiv \frac{v_c}{R}$ together with its derivative $\frac{\partial \Omega}{\partial R} = \frac{1}{R}\frac{\partial v_c}{\partial R} - \frac{v_c}{R^2}$. The radial epicycle frequency is then given by $\kappa = 2\Omega\sqrt{1 + \frac{R}{2\Omega}\frac{\partial \Omega}{\partial R}}$. Finally, recalling that the wavenumber is the derivative of the shape function introduced above, $k = \frac{\partial \psi}{\partial R}$, we can compute Toomre's number as $X \equiv \frac{k}{\kappa}\sigma_{RR}$. In our approach, Toomre's number can eventually acquire a vertical dependence trough the velocity dispersion profiles introduced above (equation 17). Because a self-consistent theory for the vertical motion of the stars in the presence of spiral arms is missing, a large freedom is left to the researcher to investigate different approaches.

After the introduction of these quantities, we are in the position to make use of the results of Lin et al. (1969). A solution of the evolution equation (i.e. the linearized Boltzmann equation) $\iota\frac{\partial f_1}{\partial t} - \mathcal{B}_0[f_1] - \mathcal{B}_1[\Phi_1] = 0$ is considered in the form:

$$f_1(\boldsymbol{x}, \boldsymbol{v}; t) = \int_{-\infty}^{t} \left\langle \nabla_{\boldsymbol{x}'}\Phi_1, \frac{\partial f^{\mathrm{Sch}}(\boldsymbol{x}', \boldsymbol{v}')}{\partial \boldsymbol{v}'} \right\rangle \mathrm{d}t', \qquad (47)$$

with natural boundary conditions $f_1 \to 0$ as $t \to +\infty$. Here, $\langle *, * \rangle$ represents the standard inner product. Under the assumption that the perturbations take the form of spiral waves $\Phi_1(\boldsymbol{x}; t) = \Phi^a(R)\mathrm{e}^{\iota(m\phi - \omega t + \int^R k\,\mathrm{d}R)}$, in a 'tightly wound' approximation, i.e. $|kR| \gg 1$, we get rapidly to the form for the perturbed DF on the plane as

$$f_1 = -\frac{\Phi_1}{\sigma_{RR}^2} f^{\mathrm{Sch}} \begin{pmatrix} 1 - \mathrm{sinc}^{-1}(\nu\pi) \times \\ \times \frac{1}{2\pi}\int_{-\pi}^{\pi} \mathrm{e}^{\iota(\nu\tau + X(u\sin\tau + v(1+\cos\tau)))}\mathrm{d}\tau \end{pmatrix}, \qquad (48)$$

with $\mathrm{sinc}^{-1}(\nu\pi) \equiv \frac{\sin(\nu\pi)}{\nu\pi}$ the 'sinc' function, where we set here for simplicity the frequency ratio $\nu \equiv \frac{\omega - m\Omega_p}{\kappa}$, and $\frac{1}{\gamma^2} \equiv \frac{\sigma_{\phi\phi}^2}{\sigma_{RR}^2} = \frac{\kappa^2}{(2\Omega)^2}$.

in agreement with the hypothesis underlying equation (18). Finally, we simplified the notation writing the peculiar velocities as $\boldsymbol{v} - \bar{\boldsymbol{v}} = \{\frac{v_R}{\sigma_{RR}}, \gamma\frac{v_\phi - v_c}{\sigma_{RR}}, \frac{v_z}{\sigma_{zz}}\} = \{u, v, w\}$.

We are ready now to proceed to compute the first-order moments of this DF that we adopted in our kinematic model. The moment of order zero and one was already carried out in numerical form by the authors in appendix A of Lin et al. (1969) to the first order, and the second-order central moments were recently proposed by Roca-Fàbrega et al. (2014) in a work focused on the vertex deviation and the bracketing of the resonances. Nevertheless, in the original work by Lin et al. (1969) and in the work Roca-Fàbrega et al. (2014), the numerical integral was passed over in favour of a more compact analytical formalism, and the divergences due to the resonances were not considered.

We present here a different solution for these moments in the form of hypergeometrical functions instead of numerical integrals. We will underline later the advantages of our formulation in the context of the present modelling approach. We will also offer a necessary solution to cover the resonances and to make the model suitable for the star-count approach that we are developing here.

6.1.1 Zero-order moments of the perturbed DF

The family of the perturbed density profiles result as the zero-order moment of the total DFs given by $f = f^{\mathrm{Sch}} + f_1$ with f^{Sch} defined by equation (46) and f_1 by equation (48). We write

$$\Sigma(R, \phi; t) \equiv \int_{\mathbb{R}^3} f\,\mathrm{d}v_R \mathrm{d}v_\phi \mathrm{d}v_z = \int_{\mathbb{R}^3}\left(f^{\mathrm{Sch}} + f_1\right)\mathrm{d}v_R \mathrm{d}v_\phi \mathrm{d}v_z. \qquad (49)$$

By exploiting the notation introduced above, we can write

$$\frac{\Sigma_1}{\Sigma_0} = \frac{\int_{\mathbb{R}^3} f_1\,\mathrm{d}v_R \mathrm{d}v_\phi \mathrm{d}v_z}{\int_{\mathbb{R}^3} f^{\mathrm{Sch}}\,\mathrm{d}v_R \mathrm{d}v_\phi \mathrm{d}v_z}$$

$$= -\frac{\Phi_1}{\sigma_{RR}^2}\frac{1}{\Sigma_0}\int_{\mathbb{R}^2}\left(1 - \mathrm{sinc}^{-1}(\nu\pi)\right. \qquad (50)$$

$$\left. \times\frac{1}{2\pi}\int_{-\pi}^{\pi}\mathrm{e}^{\iota(\nu\tau + X(u\sin\tau + v(1+\cos\tau)))}\mathrm{d}\tau\right)f^{\mathrm{Sch}}\mathrm{d}u\,\mathrm{d}v\,\mathrm{d}w,$$

and in particular, we reach the form

$$\Sigma = \Sigma_0 + \Sigma_1$$

$$= \Sigma_0 - \Sigma_0\frac{\Phi_1}{\sigma_{RR}^2}\left(\frac{1}{\Sigma_0}\frac{1}{2\pi}\int_{\mathbb{R}^3}\left(1 - \mathrm{sinc}^{-1}(\nu\pi)\right.\right. \qquad (51)$$

$$\left.\left. \times\int_{-\pi}^{\pi}\mathrm{e}^{\iota(\nu\tau + X(u\sin\tau + v(1+\cos\tau)))}\mathrm{d}\tau\right)f^{\mathrm{Sch}}\mathrm{d}u\,\mathrm{d}v\,\mathrm{d}w\right),$$

which is the obvious generalization of the work of Lin et al. (1969) to the case of vertical velocity DFs. If we remember that $\int_{\mathbb{R}^3}\frac{1}{(2\pi)^{3/2}}\mathrm{e}^{-(u^2+v^2+w^2)}\mathrm{d}u\mathrm{d}v\mathrm{d}w = 1$, the terms inside the external brackets reads simply

$$= 1 - \frac{\mathrm{sinc}^{-1}(\nu\pi)}{2\pi}\int_{\mathbb{R}^3}\mathrm{d}u\,\mathrm{d}v\,\mathrm{d}w\,\mathrm{e}^{-\frac{u^2+v^2+w^2}{2}}$$

$$\times\frac{1}{(2\pi)^{3/2}}\int_{-\pi}^{\pi}\mathrm{e}^{\iota(\nu\tau + X(u\sin\tau + v(1+\cos\tau)))}\mathrm{d}\tau. \qquad (52)$$
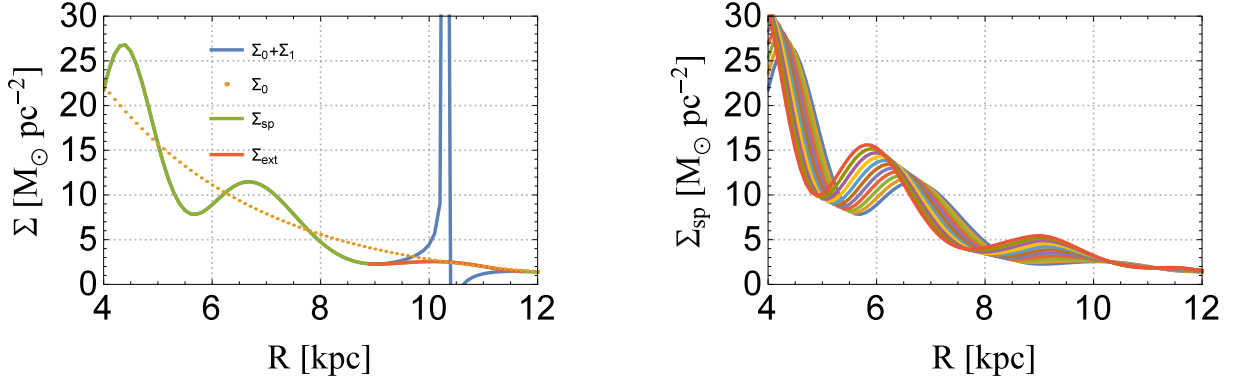
Figure 4. Left-hand panel: on-the-plane section of the perturbed density profile from equation (56) at $\phi = 0$. The blue line is the profile with singularity at the resonance location $R = R_{res}$, the red line is the analytical continuation from $R_{res} \pm \varepsilon_R$ with $\varepsilon_{res} = 1.4$kpc and the underlying green profile is the overall profile continued over the resonance (see the text for details). Right-hand panel: same green perturbed density profile of left-hand panel but for a random set of varying ϕ angles (and random colour). The purpose is just to show how smooth the passage is between one line and another at different ϕ−s.

At this point, by changing the integration order, we can obtain

$$= -\frac{\text{sinc}^{-1}(\nu\pi)}{2\pi} \frac{1}{(2\pi)^{3/2}} \int_{-\pi}^{\pi} d\tau$$

$$\times \int_{\mathbb{R}^3} du\,dv\,dw\, e^{-\frac{u^2+v^2+w^2}{2}} e^{\iota(s\tau+X(u\sin\tau+v(1+\cos\tau)))}$$

$$= -\frac{\text{sinc}^{-1}(\nu\pi)}{2\pi} \int_{-\pi}^{\pi} d\tau (e^{\iota\nu\tau-X^2(1+\cos\tau)})$$

$$= -\frac{\text{sinc}^{-1}(\nu\pi)}{2\pi} \int_{-\pi}^{\pi} d\tau e^{-X^2(1+\cos\tau)}(\cos(\nu\tau) + \iota\sin(\nu\tau)) \quad (53)$$

$$= -\frac{\text{sinc}^{-1}(\nu\pi)}{2\pi} \int_{-\pi}^{\pi} d\tau e^{-X^2(1+\cos\tau)}\cos(\nu\tau)$$

$$= -\left(\frac{1}{2},1\right) \tilde{F}_{(1-\nu,1+\nu)}(-2X^2)$$

$$\equiv -{}_{\left(\frac{1}{2},1\right)}\hat{F}_{(1-\nu,1+\nu)}.$$

Here, we introduced the generalized hypergeometric function:

$$
\begin{aligned}
{}_2\tilde{F}_2(a_1, a_2; b_1, b_2; z) &\equiv \frac{{}_2F_2(a_1, a_2; b_1, b_2; z)}{\Gamma(b_1)\Gamma(b_2)} \\
&= \frac{1}{\Gamma(b_1)\Gamma(b_2)} \sum_{k=0}^{\infty} \frac{(a_1)_k(a_2)_k}{(b_1)_k(b_2)_k} \frac{z^k}{k!},
\end{aligned} \quad (54)
$$

with $(a)_n \equiv a(a+1)\ldots(a+n-1) = \frac{\Gamma(a+n)}{\Gamma(a)}$ the Pochhammer symbol and Γ the Eulero Gamma function. In particular, we advance the notation of the hypergeometric function to

$$_{(a_1,a_2)}\hat{F}_{(b_1,b_2)} \equiv {}_2\tilde{F}_2(a_1, a_2; b_1, b_2; -2X^2). \quad (55)$$

We can then recollect the terms to express the density in a compact way as

$$
\begin{aligned}
\Sigma &= \Sigma_0 + \Sigma_1 \\
&= \Sigma_0 \left(1 - \frac{\Phi_1}{\sigma_{RR}^2}\left(1 - {}_{\left(\frac{1}{2},1\right)}\hat{F}_{(1-\nu,1+\nu)}\right)\right) \\
&= \Sigma_0 \left(1 - \frac{\Phi_1}{\sigma_{RR}^2}\frac{X^2}{1-\nu}\Re\right).
\end{aligned} \quad (56)
$$

This represents the formula for the density profile perturbed by the spiral arms that we are going to implement.

As a corollary of this result, it is evident that we are able for the first time to propose a form for the 'reduction-factor' $\Re$. This was

historically introduced in Lin et al. (1969) as the factor to which we have to reduce the response of a stellar disc below the value of a cold disc (this is presented by direct integration in Appendix A too). This compact formulation of the density perturbation due to spiral perturbations presents extremely rapid computation benefices because of the presence of the hypergeometric function ${}_2F_2$. This will turn out to be especially useful for a technique that wants to be able to realize mock catalogues, where these integrals have to be computed a larger number of times to span a huge parameter space or to realize a high number of stars by populating PDFs. The plot of the density profiles for the values of the potential of Table 2 and the parameters assumed above are in Fig. 4. As evident from the plot, the previous equation (56) presents a singularity at the resonances that we are going to treat in the next section.

6.1.2 Interpolation schemes over the resonances

As evident from Fig. 4, at the radius where the resonances are located (i.e. wherever $1 - \nu = 0$) a divergence in the density profile of Σ is present. To satisfy the normalization equation (3), we need to cover this divergence. From Fig. 4, it is evident how the closure required by the stellar population theory in equation (3) (in the special case of equation 13 and 46) leads to a failure of the normalization condition. The PDF generated by equation (56) cannot be populated in a star-count dot-by-dot fashion because of the infinite number of stars necessary to fill the locality of the radius $R = R_{res}$.

Two are the options immediately available at this point that we tested.

(i) We can apply a bilinear interpolation in cylindrical coordinates. We solve the condition of continuity $\Sigma|_{p_1} = a_{10}$ and differentiability $\{\frac{\partial\Sigma}{\partial R}, \frac{\partial\Sigma}{\partial\phi}, \frac{\partial\Sigma}{\partial R\partial\phi}\}_{p_1} = \{a_{11}, a_{12}, a_{13}\}$ in each of the four points of the grid where the potential scheme introduced above has been valued. The linear matrix for the system of 16 equations in 16 unknowns is invertible and can be solved for two radii, one internal to the Lindblad resonance $R_{res} - \varepsilon_R$, and one external to it, at $R_{res} + \varepsilon_R$. Finally the function equation (56) is extended (as the red curve in Fig. 4).

(ii) We can develop the function equation (56) on a orthogonal set of basis in cylindrical coordinates (e.g. the Bessel function J_α introduced in Section 4). Then we can mimic the behaviour of the DF $\Sigma(R) \sim \sum_{n=1}^{\infty} c_n J_{\alpha,n}(R)$ where $J_{\alpha,n}(R) \equiv J_\alpha(z_{\alpha,n}\frac{R}{R_{max}})$ and $z_{\alpha,n}$ is the zero of the Bessel function J_a, with coefficients
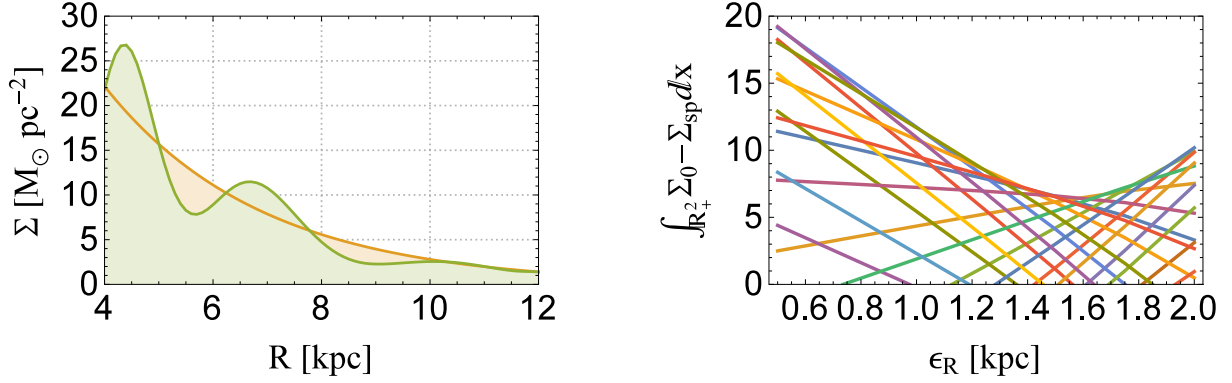
Figure 5. Left-hand panel: the integral of the continued density profile Σ_{sp} (green) and the unperturbed axisymmetric (orange). Right-hand panel: integration profile at different azimuthal directions ϕ, each for each colour, versus ε_R.

$c_n = \frac{\langle \Sigma, J_{\alpha,n} \rangle}{\langle J_{\alpha,n}, J_{\alpha,n} \rangle}$. This approach passes through a long computing of inner products and hence is very slow, it does not respect precisely the values of the original Σ and, while it can be worked out efficiently once eigenfunctions of the Laplacian operator are considered, it loses efficiency when the purpose is to cover the resonances on the velocity space.

To bypass these difficulties encountered, we developed here a general scheme that works rapidly both for the treatment of resonances on the densities (i.e. first-order moments of f^{Sch}) as well as for resonances for the moments of higher order (mean, dispersion etc.).

To achieve this goal, we proceed to investigate here a method that only extends a given profile function along the radial direction R with a polynomial P of degree $\deg(P) = 4$, i.e. $P = \sum_{i=0}^{4} c_i x^i$. The methodology can of course work equally well with $\deg(P) = 3$ to match the number of constraints at the points $P(R_{res} - \varepsilon_R)$ and $P(R_{res} + \varepsilon_R)$ where it is valued together with its derivative. Nevertheless, the same scheme with $\deg(P) = 4$, allows us to impose to the first- and second-order moments closer values to the corresponding unperturbed functions, thus allowing us to gently reduce the perturbations to the density and velocity fields to zero if desired.

The reason for this polynomial solution to work is the azimuthal symmetry of the underlying unperturbed model. As evident from the condition of resonances, $1 - \frac{m(\Omega_p - \Omega(R))}{\kappa(R)} = 0$, the divergences have no dependence on the azimuthal angle ϕ. In the framework of the DWT, we can individuate the resonances location only by analysis of the radial direction R. The results of this interpolation scheme are presented in Fig. 4 (right-hand panel), where a very close azimuthal spanning is operated to check the validity of the continuation polynomial scheme presented, with evidently satisfactory results.

The choice of the exact value that the scheme induces at the resonance is by itself a free parameter that we investigate here below.

6.1.3 The choice of the interpolating radius

The only parameter left unspecified in this interpolation scheme is the radius at which the scheme has to take over the DWT predictions. This is a single parameter, one condition is sufficient to fix it and the most natural one is based on the continuity equation. We require that the difference in mass between the continued Σ_{sp} and the unperturbed Σ_0 axisymmetric density distributions are the same (see Fig. 5)

$$\Theta(\varepsilon_R) = \int_{\mathbb{R}_+ \times [0, 2\pi[} \left(\Sigma_0 - \Sigma_{sp}(\varepsilon_R) \right) R dR d\phi. \tag{57}$$

This condition is equivalent to minimize the impact of the arbitrary shape that we chose to use to cover the resonances. If we convolve the integrals over all the angular directions we obtain Fig. 5 (right-hand panel). As is evident in the figure, the minimal difference between the integrated mass predicted by Σ_0 and Σ_{sp} is achieved for $\varepsilon_R \sim 1.5$ kpc. Finally in Fig. 6, the plot of the density profiles in the plane and above and below the plane are shown.

A black line marks the solar radius: the solar location is *assumed* to be at $\phi_\odot = 0$ but it is not a result of an investigation of any data set. So far all the values obtained in Table 2 are the results from studies in the axisymmetric formalism of Section 4. A non-axisymmetric investigation of the solar position in the MW plane is within the DWT framework is, to our knowledge, not available (and beyond the goal of this paper).

The vertical density profile of the spiral arms is not directly obtained from the DWT, which is developed only in the plane. Here, we are not searching for a self-consistent determination of the density profile, instead we assume decoupling of the vertical and radial profile in the configuration space assigning the axisimmetric density profile of the disc stellar population to the spiral arms profile too (Fig. 7).

As evidenced in the figure, the effect of the spiral arms is a tiny contraction of the vertical profile with respect to the corresponding unperturbed one. This is in response to the dependence of the density profiles to the velocity dispersions. Because of equation (9), i.e. the so-called 'age–velocity dispersion' relation evident in the MW, the older the SSP of the spiral arm is, the smaller is this contraction.

6.2 CMDs of spiral features

Once the density is computed, we know the relative contribution of all the stellar populations that we want to implement in our model (Table 1). At a given distance, we compute the synthetic photometry of an observed FOV by distributing the SSPs, or the stars, along the density profiles according to their relative contribution. The new approach presented in Section 2 allows us to use virtually any data base available in literature (and this part of the software is freely available upon request to the authors). If we want to include the treatment of the spiral arm density distribution on the photometry, the major problem is the extinction along the l.o.s. It has to be accounted for accordingly with the spiral arm distribution of the
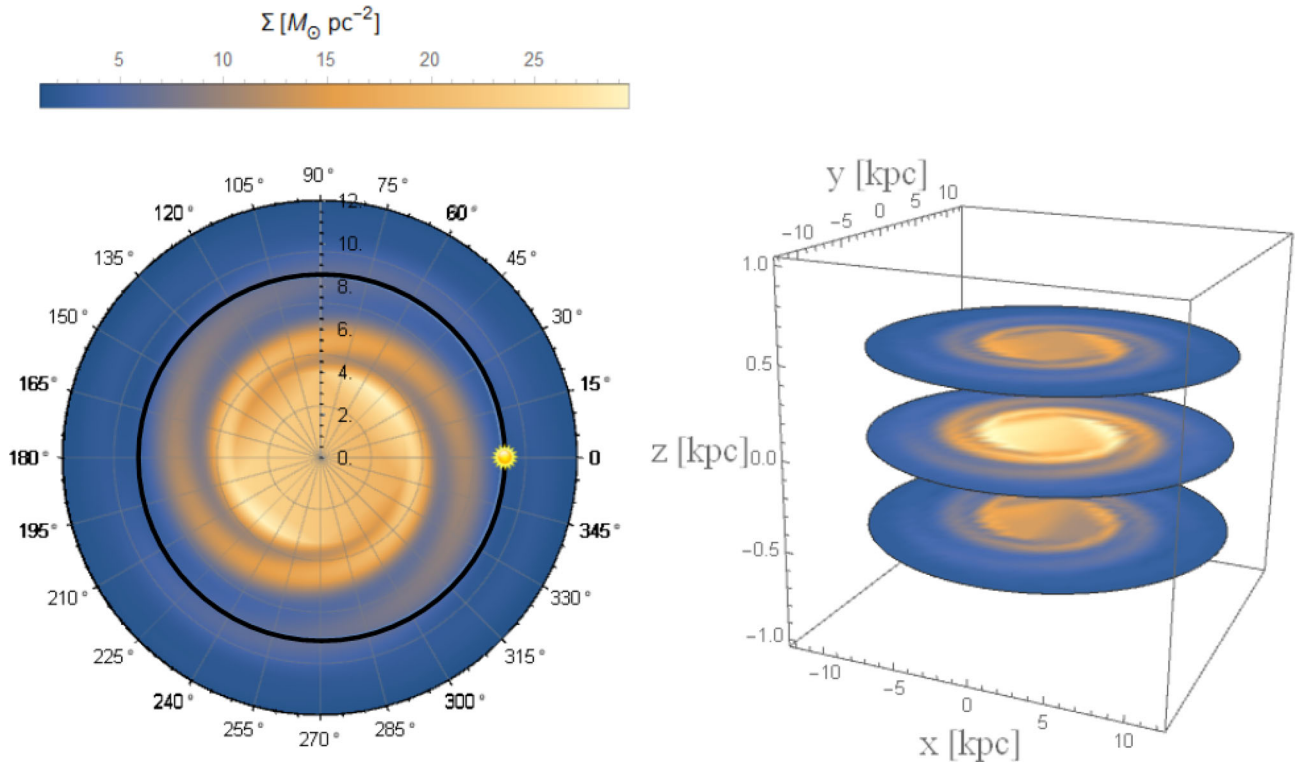
Figure 6. Left-hand panel: density profile in the plane of the MW. The Sun is located at $\{R, \phi, z\}_\odot = \{8.0, 0.0\}$[kpc]. A black circle suggests the solar radius, despite a fixed position for $\phi_\odot$ not being investigated here, it is assumed $\phi_\odot = 0$ [deg] for simplicity. The figure shows the plane at $z = 0$. Right-hand panel: out of plane density distribution for two slices symmetric below and above the plane.
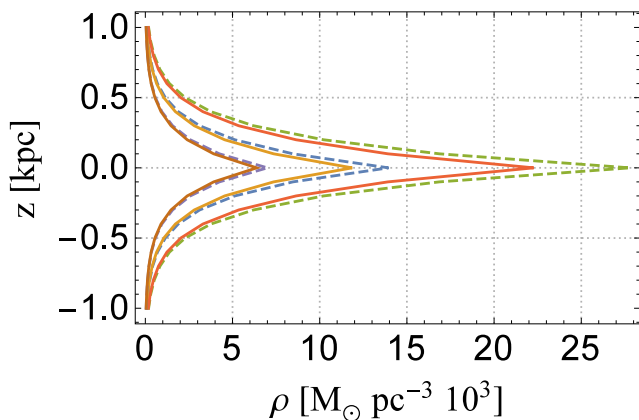

Figure 7. Vertical profile of the spiral arm component at $R = 6$, 8 and 10 kpc (solid lines). The unperturbed exponential is added for comparison with a dashed line.

stars and the gas. In particular, if we want to populate a PDF representative of a CMD for the stellar density distribution computed with the density profiles introduced above, we need an extinction model accounting for a gas distribution following the spiral arms distribution too.

To account for this extinction, we developed a model of gas distribution based on the spiral density profiles introduced above, but for cold discs ($\Re = 1$ in equation 56).

6.2.1 Extinction model

While propagating throughout a galaxy, the intensity of the star light decreases because of absorption and scattering due to the presence of interstellar dust. The combined effect, called extinction, has to be taken into account in order to derive the stars intrinsic luminosity from its observed flux. In order to predict the effect of interstellar dust on the observed CMDs, we calculated the extinction towards each SSP or each star in our model galaxy as follows.

We assumed that the dust is traced by the gas in our galaxy model and that its density, relative to the gas density (shown in Fig. 8), as well as its optical properties, are well described by the dust model of Draine & Li (2007). This dust model has been calibrated for the dust extinction curve, metal abundance depletion and dust emission measurements in the local MW. From this dust model, we consider the extinction coefficient $k_{\lambda,\text{ext}}$ per unit gas mass. From $k_{\lambda,\text{ext}}$ and the gas density distribution, ρ_{ISM}, we derive the optical depth crossed by the star light along the path between each star and the observer (located at the sun position): $\tau_\lambda = \int_\odot^* k_{\lambda,\text{ext}} \rho_{\text{ISM}} dr_{\text{hel}}$. Then, the extinction in magnitudes is derived as $A_\lambda = 2.5\tau_\lambda \log e$.

The determination of the predicted observed flux of a star taking into account dust extinction in a galaxy model is affected by several caveats. First, the optical properties of the dust are known to change substantially for different l.o.s. within the MW (e.g. Fitzpatrick 1999). Therefore, any MW dust model can only be interpreted as an average model for many directions within the Galaxy. Furthermore, the amount of obscuration due to the dust is known to change significantly between the 'diffuse' and 'dense' ISM. In particular for very young stars, still embedded in their parent molecular cloud, our approach is surely underestimating their extinction (since the Draine & Li 2007 model is calibrated for the diffuse ISM and molecular clouds are not resolved in our model for the gas distribution). In this work, we assumed that the dust follows the gas distribution within our galaxy model and that the dust optical properties are uniform. Although quite simple, this approach is sufficient to show
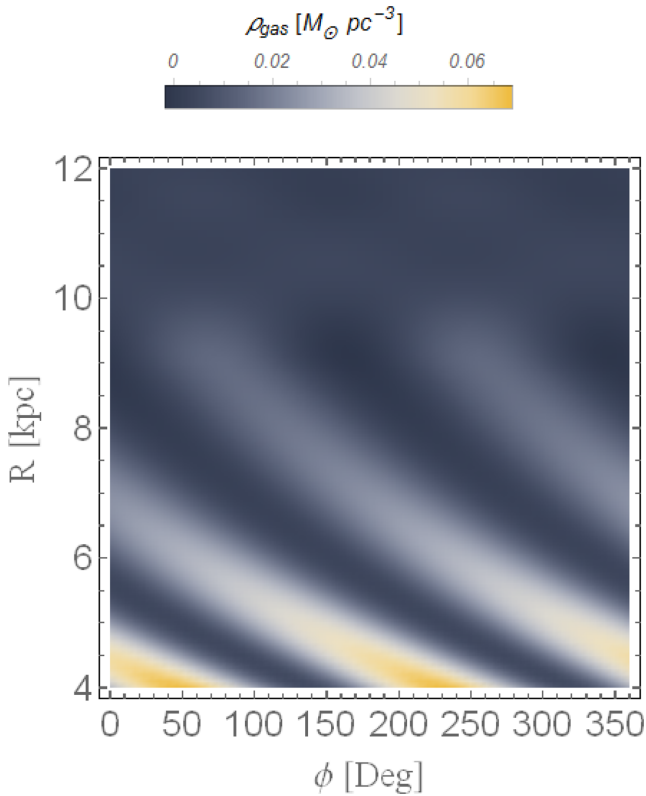
Figure 8. ISM gas distribution from equation (56). Note that this kind of density plots map a linear (i.e. R) and an angular (i.e. ϕ) quantity over square. This is causing strong distortions over the range of $R > 8$ kpc and careful attention has to be paid in its interpretation.

the general effect of the presence of spiral arms on the predicted CMD (Fig. 10).

6.2.2 Sources of stellar tracks, isochrones, SSPs in different photometric systems

We adopt the stellar models and companion isochrones and SSPs with magnitudes and colours in various photometric systems of the Padua data base because they have been widely tested and used over the years in many areas of observational stellar astrophysics going from the CMDs of stellar clusters, to populations synthesis either star-by-star or integral photometry (magnitudes and colours) or spectral energy distributions, and others.

(i) *Stellar tracks.* We will not review the physics of these stellar tracks here but we just mention that over the years, these models were calculated including semiconvection in massive stars (e.g. Chiosi & Summa 1970), ballistic-convective overshooting from the core (Bressan, Chiosi & Bertelli 1981), overshooting from the bottom of the convective envelope (Alongi et al. 1991), turbulent diffusion from the convective core and convective shells (Deng, Bressan & Chiosi 1996a,b; Salasnich, Bressan & Chiosi 1999), plus several additional improvements and revisions (Alongi et al. 1993; Bertelli et al. 1994; Fagotto et al. 1994a,b; Bertelli & Nasi 2001; Bertelli et al. 2003, 2008, 2009). The stellar models in use are those by Bertelli et al. (2008, 2009), which cover a wide grid of helium Y, metallicity Z, and enrichment ratio $\Delta Y/\Delta Z$. The associated isochrones include the effect of mass-loss by stellar wind and the thermally pulsing AGB phase according to the models calculated by Marigo & Girardi (2007).

(ii) *The data base of SSPs.* We briefly report here on the data base of isochrones and SSPs that has been calculated for the purposes of this study. The code in use is the last version of YZVAR developed over the years by the Padova group and already used in many studies (for instance Chiosi & Greggio 1981; Chiosi et al. 1986, 1989; Bertelli et al. 1995; Ng et al. 1995; Aparicio et al. 1996; Bertelli & Nasi 2001; Bertelli et al. 2003) and recently extended to obtain isochrones and SSPs in a large region of the $Z - Y$ plane. The details on the interpolation scheme at given $\Delta Y/\Delta Z$ are given in Bertelli et al. (2008, 2009). The present isochrones and SSPs are in the Johnson–Cousins–Glass system as defined by Bessell (1990) and Bessell & Brett (1988). The formalism adopted to derive the bolometric corrections is described in Girardi et al. (2002), whereas the definition and values of the zero-points are as in Marigo & Girardi (2007) and Girardi et al. (2007) and will not be repeated here. Suffice it to recall that the bolometric corrections stand on an updated and extended library of stellar spectral fluxes. The core of the library now consists of the DFNEW ATLAS9 spectral fluxes from Castelli & Kurucz (2003), for $T_{\mathrm{eff}} \in [3500, 50\,000]$ K, $\log_{10}g \in [-2, 5]$ (with g the surface gravity), and scaled-solar metallicities $[M/H] \in [-2.5, +0.5]$. This library is extended at the intervals of high T_{eff} with pure blackbody spectra. For lower T_{eff}, the library is completed with the spectral fluxes for M, L and T dwarfs from Allard et al. (2000), M giants from Fluks et al. (1994), and finally the C star spectra from Loidl, Lançon & Jørgensen (2001). Details about the implementation of this library, and in particular about the C star spectra, are provided in Marigo & Girardi (2007). It is also worth mentioning that in the isochrones we apply the bolometric corrections derived from this library without making any correction for the enhanced He content which has been proved by Girardi et al. (2007) to be small in most common cases.

The data base of SSP cover the photometric projection of any reasonable $\mathbb{E}_{\mathrm{MW}}$. The number of ages N_τ of the SSPs are sampled according to a law of the type $\tau = i \times 10^j$ for $i = 1, \ldots, 9$ and $j = 7, \ldots, 9$, and for N_Z metallicities are $Z = \{0.0001, 0.0004, 0.0040, 0.0080, 0.0200, 0.0300, 0.0400\}$. The helium content associated with each choice of metallicity is according to the enrichment law $\Delta Y/\Delta Z = 2.5$. Each SSP has been calculated allowing a small age range around the current value of age given by $\Delta \tau = 0.002 \times 10^j$ with $j = 7, \ldots, 9$. No α-enhanced or He-enhanced tracks are in use in this example (e.g. α-enhanced tracks can easily be taken from an external data base, e.g. Pietrinferni et al. 2006 or He-enhanced from Bertelli et al. 2008), and interpolated as in the previous scheme, although this extra-dimension SSP interpolation is beyond the goals of this paper focused on the kinematics of the spiral arms populations. In total, the data base contains $N_\tau \times N_Z \cong 150$ SSP. This grid is fully sufficient for our purposes. For future practical application of it, finer grids of SSPs can be calculated and made available. To calculate SSPs, one needs the IMF (see comments after equation 6) of stars of which there are many formulations in the literature. Care must be paid that the IMF of the SSPs is the same of the Galaxy model to guarantee self-consistency of the results. By construction, the IMF contains a normalization factor which depends on the IMF itself and the type of constraint one is using, e.g. the total number of stars in a certain volume, the total mass of stars in a certain galaxy component etc. In the case of an SSP, the normalization constant is usually defined imposing the total mass of the SSP to be $M_{\mathrm{SSP}} = 1\,\mathrm{M}_\odot$, so that it can immediately be used to find the total luminosity (magnitude) of a stellar assembly with a certain total mass (See Section 3 and equation 11). Needless to say that other libraries of stellar models and isochrones can be used to generate the data base of SSPs, the building blocks of our method. The same is true about
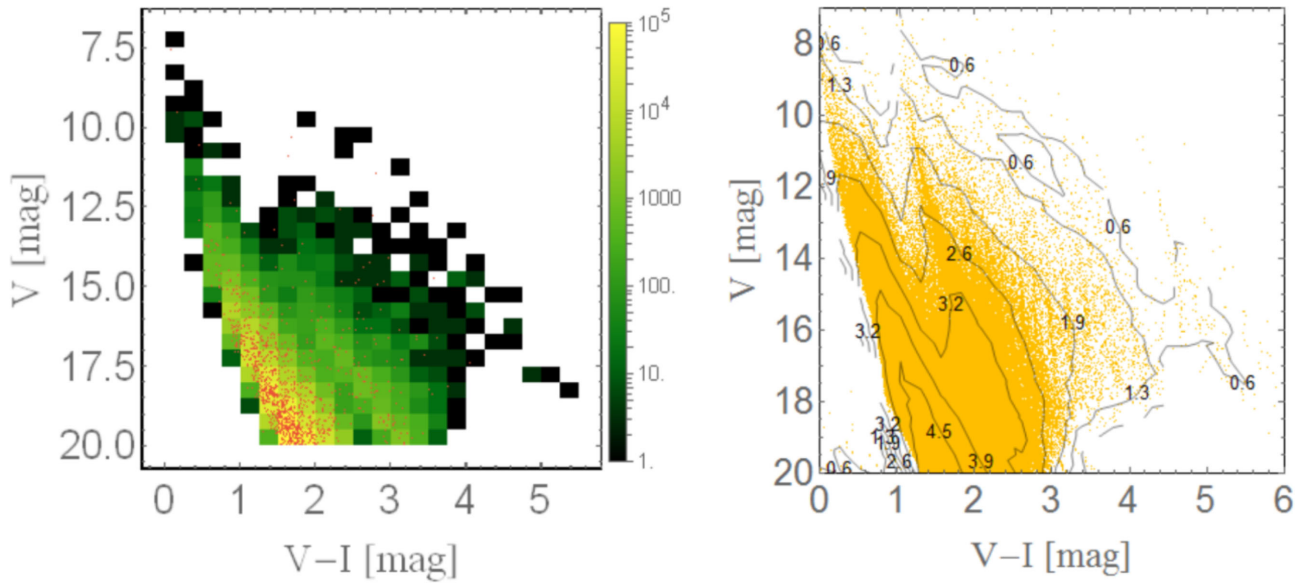
Figure 9. CMD in *V* and *I* band for a field $l \in [88, 92]°$ $b \in [-2, 2]°$ and magnitude limit $V < 20$ mag for the present model (left-hand panel) and for the Besançon model (right-hand panel, see Section 8 for details). In our model (left-hand panel), field stars are represented with PDF and only spiral arms star population is visualized in a scatter-type CMD. The logarithmic scale used in this plot is mandatory to interpret the plot and computed as explained in Section 3. For comparison, the Besançon model on the right-hand panel is presenting the classical scatter-type CMD where we overlapped the isocontour for the number of stars.

the code generating the SSPs: we have adopted our code YZVAR, of course other similar codes in literature can be used provided they may reach the same level of performance. A code generating SSPs from any data base of stellar populations is available upon request to the authors of Pasetto et al. (2012b). Equally for the photometric systems. So the matrix method for generating the DFs for starting SSPs does not depend on a particular choice for the data base of stellar tracks, isochrones, and photometric system.

(iii) *Simulation of photometric errors and completeness.* Real data on the magnitudes (and colours) of the stars are affected by photometric errors, whose amplitude in general increases at decreasing luminosities (increasing magnitude). The photometric errors come together with the data itself provided they are suitably reduced and calibrated. Photometric errors can be easily simulated in theoretical CMDs. The procedure is simple and straightforward (see for instance Pasetto et al. 2012b, for all details). To compare data acquired along a given l.o.s. with theory one has to know the completeness of the former as a function of the magnitudes and pass-band (Stetson & Harris 1988; Aparicio & Gallart 1995). This is long known problem, and tabulations of the completeness factors must be supplied in advance. The only thing to mention here is that correcting for completeness will alter the DF of stars in the cells of the observational CMD we want to analyse. These tabulations of completeness factors must be supplied by the user of our method.

(iv) *CMDs rasterization.* Modern, large surveys of stellar populations easily generate CMDs containing millions of stars or more, of different age, chemical composition, position in the host galaxy, suffering different reddening and extinction etc. so that even plotting the CMD can be a problem not to speak about deciphering it for the underlying star formation and chemical enrichment histories, mass and spatial distribution of the stellar component under examination. We have already introduced the concept PDF for a stellar population, we want now to particularize it to the case of the CMD and introduce the concept of a tessellated CMD. Given two photometric pass-bands $\delta\lambda$ and $\delta\lambda'$ and associated magnitudes

and colours, one can soon build two CMDs $m_{\delta\lambda}$ versus $m_{\delta\lambda'} - m_{\delta\lambda}$ and $m_{\delta\lambda'}$ versus $[m_{\delta\lambda'} - m_{\delta\lambda}]$ and divide this in elementary cells of size $\Delta m_{\delta\lambda}$ and $\Delta[m_{\delta\lambda'} - m_{\delta\lambda}]$. To the population of each cell contribute stars from all SSPs whose evolutionary path crosses the cell. The regions occupied by stars in the MS, red giant, red clump, and asymptotic giant phase this latter stretching to very low effective temperatures (red colours) are well evident and long lived phases display a higher number of stars compared to the short lived ones. As explained some blurring of the CMD can be caused by varying extinction across the galaxy under consideration. In the case of deep FOV, the effect of different distances for the stars is included, adding a further dimension to the problem treated with equation (11).

6.2.3 PDF versus CMDs

In Fig. 9 (left-hand panel), we present the PDF of the CMD in *V* and *I* pass-bands for an ideal field $\{l, b\}_{\mathrm{cen}} \in \{90°, 0°\}$ with opening angle $\sim2°$ and a limiting magnitude of $V < 20$ mag. We note that the PDF is not normalized to [0, 1] but by means of the integral equation (11) is normalized to the number of stars effectively predicted by the IMF, star formation history and density profiles as introduced above. The PDF of spiral arms alone has been populated by orange dots to reproduce a scatter diagram (i.e. the classical CMD) for the stellar population and superposed to the PDF distribution of the field stars. The stars in the spiral arm almost overlap with the MS stars of the field. The faint evolved sequence is visible at the right of the MS. The right-hand panel shows the distribution of stars in the analogous field generated by the Besançon model[1] where standard scatter plots are used for the CMDs. A detailed comparison of the kinematics of the MW stellar populations in our model and in the Besançon model is left for Section 8. Here, we want to

---

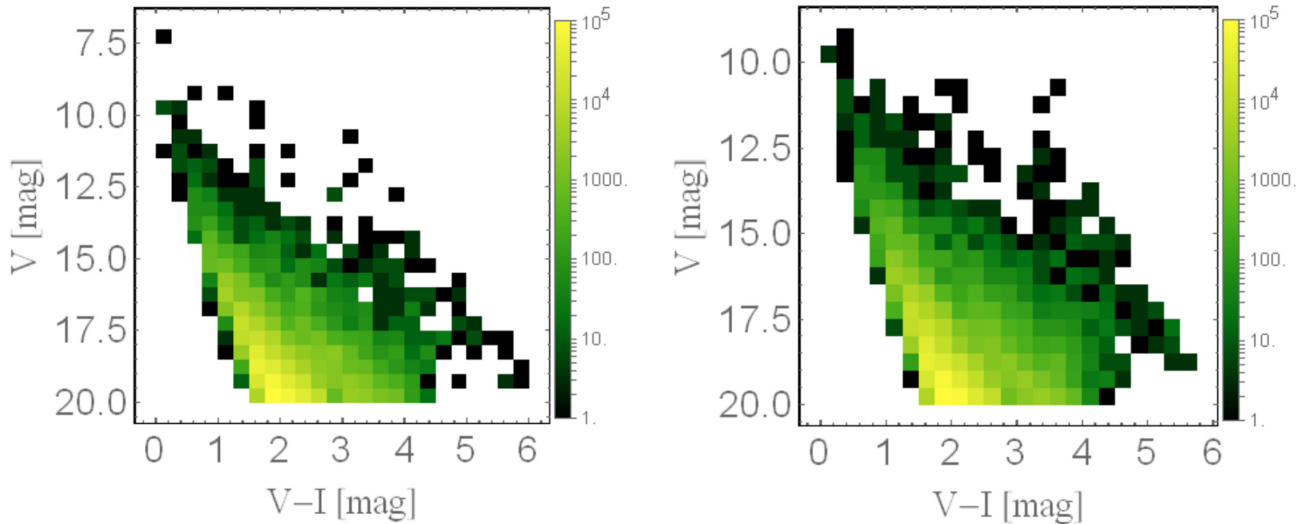[1] Online version of the 2013 July 5, 9:46 CEST.

Figure 10. Left-hand panel: CMD for the sole field stellar population derived by using the extinction model introduced in Section 6.2.1. Right-hand panel: CMD realized assuming a double exponential extinction profile on the sole field stars.

point out how our technique (presented in Pasetto et al. 2012b) is particularly fast because of the use of PDFs as opposite to the scatter diagrams used in the Besançon model. This is a key feature of our model and it is particularly suited to deal with the upcoming era of large surveys where the realization of several CMDs per second is necessary in order to explore large parameter spaces. Vice versa this exploration seems to be a practical impossibility in models such as the Besançon (if not by involving heavy parallel calculus machines) where the techniques requires the realization of scatter plots with dots-over-dots plotted in each colour–magnitude square (cf. explanation in Section 3). Clearly from the Besançon model, we can reach the same PDF distribution presented in our technique (e.g. by binning the scatter plot in the right-hand panel of Fig. 9) but the two models work fundamentally in the opposite direction. Our modelling approach works by generating convolved PDFs and then (if necessary) by populating them to obtain a scatter plot, vice versa the Besanç model works by obtaining first the scatter plots diagrams and then (if necessary) by binning them to have PDF.

Finally, in Fig. 10 we show two examples of tesselated CMDs for a population of field stars observed in the *V* and *I* pass-bands and in which two different extinction profile have been adopted. The left-hand panel shows the case with extinction represented by the asymmetric gas spiral distribution of Fig. 8, whereas in the right-hand panel two exponential laws are used for the extinction. The logarithmic colour code is proportional to the value of the PDF in each cell. Once the stars are distributed on the CMD, we can test the effect of the new extinction model. The large impact of the gas distribution along the spiral arms in shaping the composite CMD is soon evident. Analysing this particular field in more detail is beyond the goal of the present study. However, it is worth mentioning that the combined effects of the large viewing angle and the density gradient in mass density due to spiral arms have combined to stretch the distribution of stars to the red side of the CMD. This is because of the more concentrated gas/dust distribution rising up rapidly at about 1.3 kpc from the solar position along the l.o.s. In a near future, surveys like *Gaia* will be able to provide great insight on the distribution of gas and dust across the MW. In this context, the technique we have developed can

soon be adapted to a star-by-star approach to directly determine the extinction.

7 VELOCITY FIELD DESCRIPTION OF NON-AXISYMMETRIC FEATURES: AZIMUTHAL AND VERTICAL TILT OF THE VELOCITY ELLIPSOID

The tilt of the velocity ellipsoid with respect to the configuration space axis generates non-null diagonal terms in the matrix $\boldsymbol{\sigma}_v(\boldsymbol{x})$ introduced in equation (46). We derive here these non-null terms in the context of two independent theories.

Following what was done for the zero-order moment of f^{Sch}, we rely on the DWT to derive the moments of order one or more for the velocity field on the plane, and on the study by Amendt & Cuddeford (1991) for the velocity moments on the meridional plane.

Finally once the moments of the velocity DF are obtained, the velocity of the field is derived from the diagonalization of $\boldsymbol{\sigma}_v(\boldsymbol{x})$ by simply solving the eigen-system:

$$\det(\boldsymbol{\sigma}^{-1} - \lambda \boldsymbol{I}) = 0, \tag{58}$$

with $\boldsymbol{I}$ the unit matrix and λ the eigenvalues, and populating the corresponding tilted PDF.

7.1 Radial-azimuthal velocity field

7.1.1 Radial mean stream velocity

The computation of the velocity field proceeds exactly as above for the moment of order zero. We start with the radial moment defined as

$$
\begin{aligned}
\bar{v}_R &= \frac{1}{\Sigma} \int_{\mathbb{R}^3} f v_R \mathrm{d}v_R \mathrm{d}v_\phi \mathrm{d}v_z \\
&= \frac{\Sigma_0}{\Sigma} \bar{v}_{0,R} + \frac{\Sigma_0}{\Sigma} \frac{1}{\Sigma_0} \int_{\mathbb{R}^3} f_1 v_R \mathrm{d}v_R \mathrm{d}v_\phi \mathrm{d}v_z \\
&= \frac{1}{\Sigma} \int_{\mathbb{R}^3} f_1 v_R \mathrm{d}v_R \mathrm{d}v_\phi \mathrm{d}v_z,
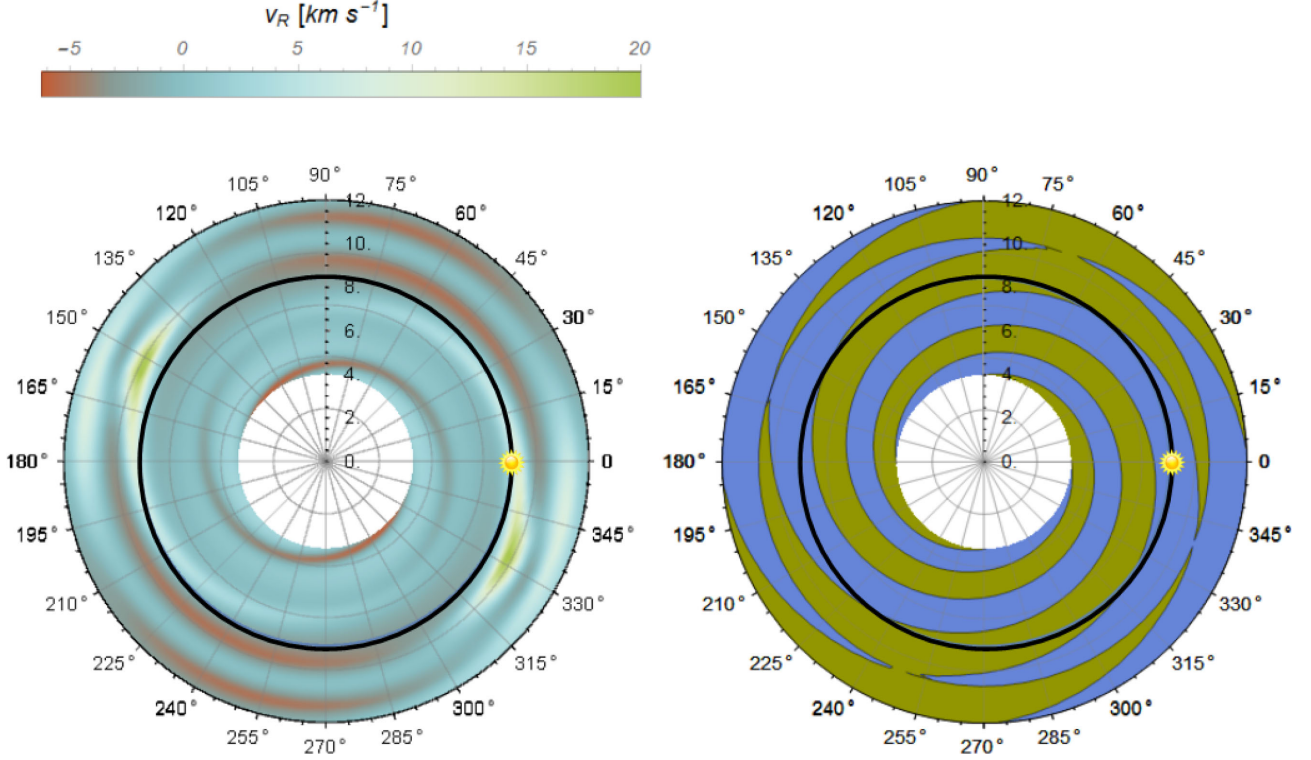\end{aligned}
\tag{59}
$$

Figure 11. Left-hand panel: mean radial velocity $\bar{v}_R$ for a spiral stellar population. The Sun is arbitrarily located at $\{R, \phi, z\}_\odot = \{8.0, 0.0, 0.02\}$[kpc, deg, kpc] and its circle radius shown in black. The figure is on the plane at $z = 0$. Right-hand panel: density contrast $\Sigma_{\rm sp} - \Sigma_0$ at one contour level. Density contrast is negative in blue-colour.

where $\bar{v}_{0,R} = \frac{1}{\Sigma_0} \int f^{\rm Sch} v_R \mathrm{d}v_R \mathrm{d}v_\phi \mathrm{d}v_z = 0$ and remembering equation (48) we evidently need to compute the following

$$\bar{v}_R = -\frac{\Sigma_0}{\Sigma} \frac{\Phi_1}{\sigma_{RR}^2} \frac{1}{\Sigma_0} \int_{\mathbb{R}^3} f^{\rm Sch} \left(1 - \frac{{\rm sinc}^{-1}(\nu\pi)}{2\pi} \right.$$
$$\left. \times \int_{-\pi}^{\pi} e^{\iota(\nu\tau + X(u \sin\tau + v(1+\cos\tau)))} \mathrm{d}\tau \right) u \frac{\sigma_{RR}^3}{\gamma} \sigma_{zz} \mathrm{d}u\mathrm{d}v\mathrm{d}w. \tag{60}$$

But the RHS of the previous equation reads

$$= -\frac{\Sigma_0}{\Sigma} \frac{\Phi_1}{\sigma_{RR}^2} \frac{1}{\Sigma_0} \frac{\sigma_{RR}^3}{\gamma} \sigma_{zz} \left(\int_{\mathbb{R}^3} f^{\rm Sch} u\mathrm{d}u\mathrm{d}v\mathrm{d}w - \int_{\mathbb{R}^2} f^{\rm Sch} \right.$$
$$\left. \times \frac{{\rm sinc}^{-1}(\nu\pi)}{2\pi} \int_{-\pi}^{\pi} e^{\iota(\nu\tau + X(u \sin\tau + v(1+\cos\tau)))} \mathrm{d}\tau \right) u\mathrm{d}u\mathrm{d}v\mathrm{d}w, \tag{61}$$

where the first term in the round brackets is identically null because no average radial motion is expected on an axisymmetric disc. We simplify further equation (60) by introducing explicitly equation (46) as

$$\bar{v}_R = \frac{\Sigma^{\rm Sch}}{\Sigma} \frac{\Phi_1}{\sigma_{RR}} \frac{{\rm sinc}^{-1}(\nu\pi)}{(2\pi)^2} \int_{-\pi}^{\pi} \mathrm{d}\tau$$
$$\times \int_{\mathbb{R}^2} \mathrm{d}u\mathrm{d}v\mathrm{d}w e^{\iota(\nu\tau + X(u \sin\tau + v(1+\cos\tau)))} u e^{-\frac{u^2+v^2+w^2}{2}}, \tag{62}$$

so that carrying out explicitly the integral on the bottom row of the previous equation we get

$$\bar{v}_R = \frac{\Sigma_0}{\Sigma} \frac{\Phi_1}{\sigma_{RR}} \frac{X}{2\pi} {\rm sinc}^{-1}(\nu\pi) \int_{-\pi}^{\pi} \mathrm{d}\tau \iota \sin\tau e^{\iota\nu\tau - X^2(1+\cos\tau)}, \tag{63}$$

and finally, making use of the equation (53), we are able to write the first-order moment in the radial direction as

$$\bar{v}_R = \frac{\Sigma_0}{\Sigma} \frac{\Phi_1}{\sigma_{RR}} \frac{X}{2} {\rm sinc}^{-1}(\nu\pi)$$
$$\times \left(\left(\tfrac{1}{2},1\right) \hat{F}_{(-\nu,2+\nu)} - \left(\tfrac{1}{2},1\right) \hat{F}_{(\nu,2-\nu)} \right). \tag{64}$$

We plot an example of the computing of equation (64) in Fig. 11. As evidenced in the moment of order zero, the amplitude of the response in the velocity field at the resonances grows beyond the limits permitted by the linear response theory of Lin et al. (1969) and the theory breaks down. Analytical continuation is applied also in this case within the same framework developed for the first-order moment above. For a spiral pattern with trailing spiral arms, $i > 0$, it is easy to prove that the wavenumber $k = \frac{\partial\psi}{\partial R} < 0$ and so ψ is a decreasing function of R. Hence, for example, if we are considering the regions where $\Omega_p > \Omega(R)$ (see also Fig. 6) we have that $\nu > 0$. Inside the spiral arm, it is $\Sigma_1 > 0$ so that we must have $\Phi_1 < 0$. Hence, with the centre of the spiral being given by the phase $\varphi = 0$, we recover the results expected by the density spiral wave theory that presents mean radial motion towards the Galactic Centre inside the spiral arm and a motion outwards in the interarm regions $\varphi = \pm\pi$ depending on the location where $\Omega_p = \Omega(R)$ as shown in Fig. 11 just above the $\sim$6.5 kpc (Faure, Siebert & Famaey 2014). As evidenced by the one contour style of this figure where $\Sigma_{\rm sp} - \Sigma_0$ has been plotted, the mean radial velocity field of Fig. 11 is in-phase with the density as expected from DWT. This test is not only performed to graphically validate the computation of the velocity moments through hypergeometric functions, but more importantly, to evidence the goodness of the continuation scheme of Section 6.2.1 over the resonance on the velocity space. As evident
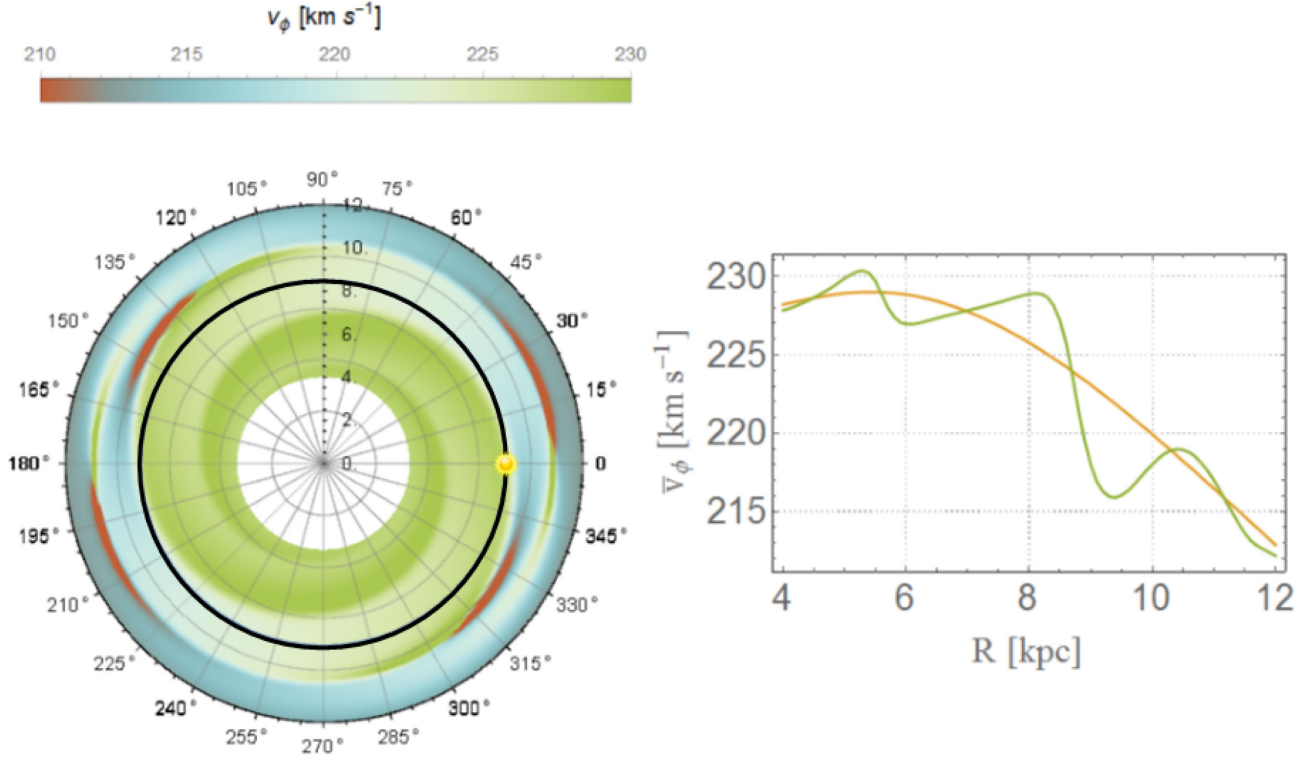
Figure 12. Left-hand panel: mean stream azimuthal velocity over all the disc. Right-hand panel: mean stream azimuthal velocity for spiral arm distributed SSP (green). It's evident the strong influence of the spiral arms in the measure circular velocity (see the text for detail). For comparison, the rotation curve of Fig. 3 is added in the range of interest of the spiral arms.

from the plot, the expectation holds even above and very close to the resonances, $R \in [R_{\mathrm{res}} - \varepsilon_{\mathrm{res}}, R_{\mathrm{res}} + \varepsilon_{\mathrm{res}}]$, a result which is not obvious to prove analytically.

7.1.2 Azimuthal mean velocity

It is even more interesting to describe the influence of the spiral arms in the mean azimuthal velocity for its implications regarding the location of the Sun relative to the local standard of rest. Because of the similarity of the integrations performed previously in the radial direction, we report here simply the results. We obtain for the azimuthal direction

$$\bar{v}_\phi = \frac{\Sigma^{\mathrm{Sch}}}{\Sigma} v_c - \frac{\Sigma^{\mathrm{Sch}}}{\Sigma} \Phi_1 \frac{v_c}{\sigma_{RR}^2} \left(1 - \frac{\nu\pi}{\sin(\nu\pi)} \left(\tfrac{1}{2}, 1 \right) \hat{F}_{(1-\nu,1+\nu)} \right),$$

(65)

that we plot on Fig. 12. As shown in this figure, the average azimuthal perturbation on the circular velocity is of the order of 5–10 km s^{-1}, i.e. compatible with the motion of the sun relative to the LSR. This result is extremely interesting no matter where the resonance is located. At every radius, the spiral arm presence affects the mean motion and can severely bias the works aimed to determine the motion of the Sun with respect to the circular velocity (the local standard of rest). This is in line with what is already evidenced by numerical simulations (e.g. Quillen & Minchev 2005; Faure et al. 2014; Kawata et al. 2014). Unfortunately, up to now the result has only a theoretical value because it is affected by the uncertainties on the resonances' locations, on the validity of the DWT, and on the uncertainty of the Sun's location.

7.1.3 Dispersion velocity tensor

The moments of order two can be calculated by direct integration, but the procedure is more cumbersome and the integrals not easily tractable analytically. A simpler and fully algebraic procedure is followed here bypassing the direct integration in favour of the second order not central moments. The desired results will be then achieved with the help of the previously obtained equations (64) and (65). We present here the computation for the first of these moments; the results for the following orders are obtainable following a similar procedure. From the definition of non-central radial moment of order two we write

$$
\begin{aligned}
\overline{v_R^2} &= \frac{1}{\Sigma} \int_{\mathbb{R}^3} f v_R^2 \mathrm{d}v_R \mathrm{d}v_\phi \mathrm{d}v_z \\
&= \frac{1}{\Sigma} \int_{\mathbb{R}^3} \left(f^{\mathrm{Sch}} + f_1 \right) v_R^2 \mathrm{d}v_R \mathrm{d}v_\phi \mathrm{d}v_z \\
&= \frac{\Sigma_0}{\Sigma} \sigma_{RR}^2 + \frac{1}{\Sigma} \int_{\mathbb{R}^3} f_1 v_R^2 \mathrm{d}v_R \mathrm{d}v_\phi \mathrm{d}v_z,
\end{aligned}
$$

(66)

and remembering the definition of f_1 from equation (48) we obtain

$$
\begin{aligned}
\overline{v_R^2} &= \frac{\Sigma_0}{\Sigma} \sigma_{RR}^2 - \frac{1}{\Sigma} \frac{\Phi_1}{\gamma} \frac{\sigma_{zz}}{\sigma_{RR}^{-2}} \int_{\mathbb{R}^3} \frac{\Sigma_0}{(2\pi)^{3/2} \sigma_{RR} \sigma_{\phi\phi} \sigma_{zz}} \\
&\quad \times e^{-\frac{u^2+v^2+w^2}{2}} \left(1 - \frac{\mathrm{sinc}^{-1}(\nu\pi)}{2\pi} \times \frac{}{\int_{-\pi}^{\pi} e^{u(\nu\tau + X(u\sin\tau + v(1+\cos\tau)))} \mathrm{d}\tau} \right) u^2 \mathrm{d}u \mathrm{d}v \mathrm{d}w \\
&= \frac{\Sigma_0}{\Sigma} \sigma_{RR}^2 - \frac{\Sigma_0}{\Sigma} \Phi_1 \left(1 - \mathrm{sinc}^{-1}(\nu\pi) \left(\left(\tfrac{1}{2}, 1 \right) \hat{F}_{(1-\nu,1+\nu)} \right. \right. \\
&\quad \left. \left. -2X^2 \left({}_{(3/2,2)} \hat{F}_{(2-\nu,2+\nu)} - 3 \, {}_{(5/2,3)} \hat{F}_{(3-\nu,3+\nu)} \right) \right) \right).
\end{aligned}
$$

(67)

In the same way, we obtain for the azimuthal term (the computation is tedious but straightforward):

$$\overline{v_\phi^2} = \frac{\Sigma_0}{\Sigma} v_c^2 \left(1 - \frac{\Phi_1}{\sigma_{RR}^2} \left(1 - \frac{\nu\pi}{\sin(\nu\pi)} \, _{(\frac{1}{2},1)}\hat{F}_{\{1-\nu,1+\nu\}} \right) \right), \tag{68}$$

and for the mixed term:

$$\overline{v_R v_\phi} = \frac{\Phi_1}{\sigma_{RR}} \frac{\Sigma_0}{\Sigma} \frac{\mathrm{sinc}^{-1}(\nu\pi)}{2} \frac{X}{\gamma} \\ \times \left(\gamma v_c \left(_{(1/2,1)}\hat{F}_{(-\nu,\nu+2)} - _{(1/2,1)}\hat{F}_{(\nu,2-\nu)} \right) \right. \\ \left. + \iota X \sigma_{RR} \left(_{(3/2,2)}\hat{F}_{(1-\nu,\nu+3)} - _{(3/2,2)}\hat{F}_{(\nu+1,3-\nu)} \right) \right). \tag{69}$$

The computing of these terms results from a simple application of the hypergeometric formalism introduced above. The last step to achieve the dispersion velocity terms for the velocity ellipsoid perturbed by spiral arms comes as a simple collection of the previous results as

$$\sigma_{RR} = \overline{v_R^2} - \bar{v}_R^2,$$
$$\sigma_{\phi\phi} = \overline{v_\phi^2} - \bar{v}_\phi^2, \tag{70}$$
$$\sigma_{R\phi} = \overline{v_R v_\phi} - \bar{v}_\phi \bar{v}_R,$$

and with equations (69), (68), (67), (65), and (64), we conclude the computation of the second-order moments.

Of particular interest is for example the plot of the mixed term $\sigma_{R\phi}$ because of its connection with the azimuthal tilt (of an angle l_v) with respect the configuration space cylindrical coordinates of the velocity ellipsoid on the plane:

$$l_v(R, \phi, z) = \frac{1}{2} \arctan \left(\frac{2\sigma_{R\phi}^2}{\sigma_{RR}^2 - \sigma_{\phi\phi}^2} \right), \tag{71}$$

i.e. the vertex deviation that we plot in Fig. 13. There is much observational evidence for the dependence of the tilting of the velocity ellipsoid on the plane (since Lindblad 1958; Woolley 1970) and recently it has been studied in Pasetto et al. (2012d). In the latter work, a detailed plot of this trend has been shown not only on the plane but also above and below the plane. These data based on the RAVE survey highlight a decrease of the vertex deviation above and below the plane. This observational trend is important to validate the vertical treatment of the vertex deviation outside the plane. Because the theory is not self-consistently validated outside the plane, we point out that the dependence on 'z' of equation (71) comes from the vertical dependence of $\sigma_{R\phi}$, σ_{RR} and $\sigma_{\phi\phi}$. While the behaviour of σ_{RR} and $\sigma_{\phi\phi}$ outside the plane are given by equation (17), which find observational constraints in the values in Table 1, the trend of $\sigma_{R\phi} = \sigma_{R\phi}(z)$ is entirely a simplified assumption we adopted in equation (70). The results of the convolution of just two SSPs of pop 1 and pop 2 of Table 2 (Fig. 14) treated with DWT seem to qualitatively reproduce the observational trend of Pasetto et al. (2012d, their left-hand panel in Fig. 12).

7.1.4 Limits of the adopted approach

Even if the tilt of the velocity ellipsoid presents a regular trend, the present theory accounts only for the contribution of the spiral arms which is well known to be incomplete. The stream motions are expected to have major impact on the velocity distribution in the solar neighbourhood as proven by several authors (e.g. Woolley 1970; Mayor 1972; Hilton & Bash 1982; Bassino, Dessaunet & Muzzio 1986; Dehnen 1999b; Soubiran et al. 2003; De Simone, Wu & Tremaine 2004; Seabroke & Gilmore 2007). In order to
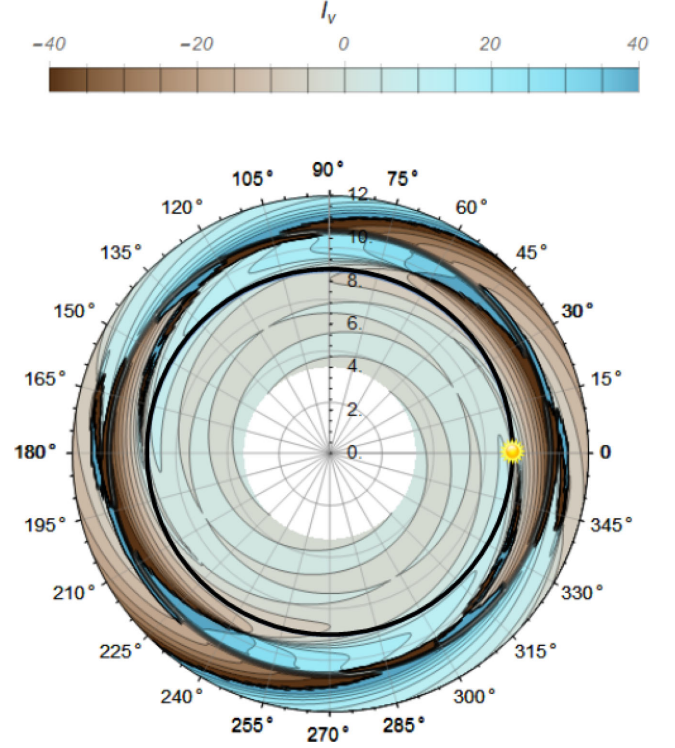
Figure 13. Vertex deviation of the velocity ellipsoid at the plane. No graphical smoothing is applied in the contour plot to evidence the grid resolution adopted.
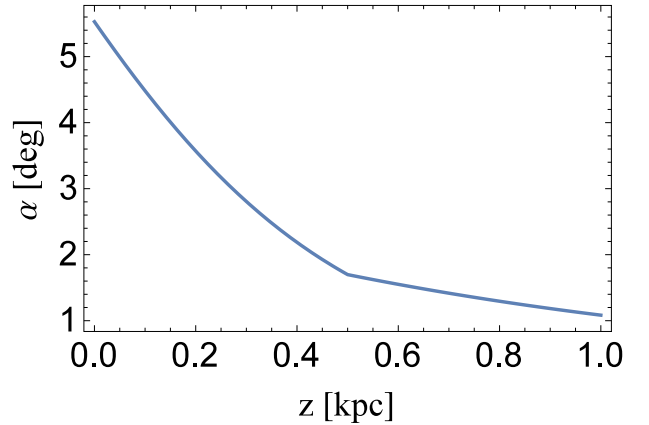

Figure 14. Vertex deviation outside the plane on the solar radial position $l_v = l_v(R_\odot, 0, z)$.

correctly account for the tilt, a complete map of the distribution of the molecular clouds encountered by the stars along their past orbits is needed. To date, this target is out of reach thus weakening any study of the kinematics and dynamics of MW based on direct orbit-integration. This is one of the main reasons spurring us to apply the method of moments in our model of the Galaxy. A limitation of our approach is surely the lack of a self-consistent treatment of the vertical DF. The DWT is limited to in-plane stellar motions (the vertical and planar motions are uncoupled because of the epicyclical approximation). This represents a serious drawback of the theory that makes it not fully coherent with the assumptions we are going to make on the vertical tilt of the velocity ellipsoid. None the less, we will include the vertical tilt in the Galaxy model because, as shown

in Fig. 14, our approach seems to capture, at least qualitatively, the information hidden in the observational data acquired by Pasetto et al. (2012d).

7.2 Vertical velocity field

The study of the local vertical profiles of the MW discs has long tradition and is still pushed mostly under axisymmetric assumption (e.g. Siebert, Bienaymé & Soubiran 2003; Soubiran et al. 2003; Bienaymé et al. 2006; Soubiran et al. 2008; Just & Jahreiß 2010; Just, Gao & Vidrih 2011). The study of the vertical kinematics of spiral arms is still an open research field (e.g. Widrow et al. 2012; Williams et al. 2013). The kinematical description of the implemented model outside the plane is formally obtained here for the axisymmetric case. Nevertheless, the tilt of the velocity outside the plane and the non-isothermality for single SSP reduce to zero thus matching the in-plane description presented in the previous section.

7.2.1 Vertical tilt of the velocity ellipsoid

The last non-null cross term considered in equation (43) is $\sigma_{Rz}^2 = \sigma_{Rz}^2(R, \phi, z)$. It represents the tilt of the principal axis of the velocity ellipsoid with respect to cylindrical coordinates outside the plane. By symmetry in any axisymmetric model we expect that $\sigma_{Rz}^2(R, 0) = 0$, so that the principal axes of the velocity ellipsoid are aligned with the cylindrical coordinates in the plane. This is not generally true in a non-axisymmetric model or in a model with non-null radial average velocity (Cubarsi 2014a,b). Out of the plane the alignment is poorly known. For small z, we can write

$$\sigma_{Rz}^2\left(R_\odot, z\right) \approx \sigma_{Rz}^2\left(R_\odot, 0\right) + z\frac{\partial\sigma_{Rz}^2\left(R_\odot, 0\right)}{\partial z} + O\left(z^2\right), \quad (72)$$

where $\sigma_{Rz}^2(R_\odot, 0) = 0$ if and only if the model is axisymmetric. The z-derivative of σ_{Rz}^2 (the last term of equation 72) evaluated on the plane gives the orientation of the velocity ellipsoid just above or below the plane. Eddington (1915) and Dejonghe & de Zeeuw (1988) have shown that the velocity tensor is diagonal in coordinates (if they exist) in which the potential is separable. In the case where the MW potential is separable in cylindrical or spherical coordinates, corresponding to mass distributions which are highly flattened and dominated by the disc or spherical halo, we recover the limiting case of the vertical titling of the velocity ellipsoid (Ghosh, Bhattacharjee & Cowsik 1989; Evans, de Zeeuw & Lynden-Bell 1990; Hunter et al. 1990; Merritt & Stiavelli 1990; Dejonghe & Laurent 1991; Evans & de Zeeuw 1992; Osipkov 1994; Arnold 1995; Mathieu & Dejonghe 1996; Bienaymé 1999; Verolme & de Zeeuw 2002; Famaey & Dejonghe 2003; Helmi, White & Springel 2003; van de Ven et al. 2003).

These two cases correspond to the upper and lower boundaries of the tilt term. They are usually written as

$$\frac{\partial\sigma_{Rz}^2(R, 0)}{\partial z} = \lambda(R)\frac{\sigma_{RR}^2(R, 0) - \sigma_{zz}^2(R, 0)}{R}, \quad (73)$$

where $\lambda(R) \in [0, 1]$. The factor $\lambda(R)$ can be derived either analytically from orbit integration or is assumed $\lambda = 0$ for simplicity (e.g. van der Kruit & Freeman 1986; Lewis & Freeman 1989; Sackett & Sparke 1990). Numerical simulations (e.g. Carlberg & Innanen 1987; Bienaymé 2000) are performed to calculate explicitly the moments for a given gravitational potential. The result of the above studies is that, at the Sun's position $\lambda \simeq 0.5$. In our model for the

Galactic kinematics, we prefer to adopt the analytical formulation of $\lambda(R)$ given by Amendt & Cuddeford (1991):

$$\lambda(R) = \left.\frac{R^2\partial_{R,z,z}\Phi}{3\partial_R\Phi + R\partial_{R,R}\Phi - 4R\partial_{z,z}\Phi}\right|_{(R,z=0)}. \quad (74)$$

The expression (74) is null for a potential separable in cylindrical coordinates because the term $\frac{\partial\Phi_{\text{tot}}}{\partial R\partial z^2} = 0$. In spherical coordinates $\lambda = 1$, the relation (73) will be used in the following to describe the tilt of the velocity ellipsoid, obtaining for the DM halo

$$\lambda_{\text{DM}}(R) = -\frac{R^2}{R^2\left(q_\Phi^2 - 2\right) + 2h_{r,\text{DM}}^2\left(q_\Phi^2 - 1\right)}, \quad (75)$$

and similarly, a unitary constant value for the bulge and stellar halo components is estimated. Finally, for the important contribution of the disc we simplify equation (73) as

$$\lambda_D(R) = -\int_0^\infty \frac{kR^2J_1(kR)h_z^{-1}\text{d}k}{R\left(k - \frac{4}{h_z}\right)J_0(kR) + 2J_1(kR)} \quad (76)$$

that has to be included in equation (73) with a sum over all the discs components.

Finally, we close this section noting that the vertical tilt in the azimuthal-z direction, i.e. $\sigma_{\phi z}$, has no clear global trend in dependence on the configuration space $\sigma_{\phi z} = \sigma_{\phi z}(R, \phi, z, \text{e.g.}$ Pasetto et al. 2012d), hence we simply assume here globally $\sigma_{\phi z} = \text{const.} = 0.0$. This does not mean that locally $\sigma_{\phi z}$ has to be zero: velocity active regions (e.g. Feitzinger & Spicker 1986) especially in relation to galactic fountains, minor mergers of dwarf galaxies absorbed by the MW and globular clusters passing throughout the MW disc can easily produce areas of the MW discs where $\sigma_{\phi z} \neq 0.0$ as well as $\sigma_{\phi z} \neq \sigma_{z\phi}$ if large magnetic fields are present.

7.2.2 Non-isothermal profile of the Galactic discs

It is common to assume that the velocity distribution is isothermal in the vertical direction, or more precisely that $\frac{\partial\sigma_{zz}^2}{\partial z} = 0 \,\forall f_{\text{SSP}}$ as we have already done in Section 7.1. This is certainly a reasonable assumption for small z, although there is no reason why the galactic disc should be isothermal at all. Bahcall (1984b, but see also Bahcall 1984a; Bahcall & Soneira 1984) treated the problem assuming that non-isothermality can be simulated by the superposition of more isothermal components. The observations of Kuijken & Gilmore (1989a,b,c) show significant departures from isothermality at large z. One can prove (Amendt & Cuddeford 1991) that in a cool disc $\sigma_{Rz}^2 = -\sigma_{zz}^2\frac{\partial\sigma_{zz}^2}{\partial z}(\frac{\partial\sigma_{zz}^2}{\partial R})^{-1}$. This tells us immediately that if the tilt term of the ellipsoid is zero, then the velocity dispersion is constant in the vertical direction. Therefore, the assumption of an isothermal structure for f_{SSP} is true only in the case of a gravitational potential which is separable in cylindrical coordinates. In the case of no strict isothermality, this approximation is valid within 1 kpc from the plane, where the fractional change in σ_{zz}^2 is expected to be less than 3 per cent (Amendt & Cuddeford 1991; Cuddeford & Amendt 1991). For all reasonable gravitational potentials, $\sigma_{RR}^2 > \sigma_{zz}^2$ and one can prove that σ_{zz}^2 has an extremum (minimum) on the plane, i.e. first derivative null $\frac{\partial\sigma_{zz}^2}{\partial z} = 0$ (Hill, Hilditch & Barnes 1979; Fuchs & Wielen 1987; van der Kruit 1988; Wainscoat, Freeman & Hyland 1989). For small z and fixed $R = R_\odot$, one can perform the Taylor expansion $\sigma_{zz}^2(R_\odot, z) \simeq \sigma_{zz}^2(R_\odot, 0) + \frac{1}{2}z^2\frac{\partial^2\sigma_{zz}^2(R_\odot)}{\partial z^2} + o(z^3)$. Assuming now that $\sigma_{RR}^2(R_\odot, 0) = \alpha \cdot \sigma_{zz}^2(R_\odot, 0)$ as for Section 7.1, one
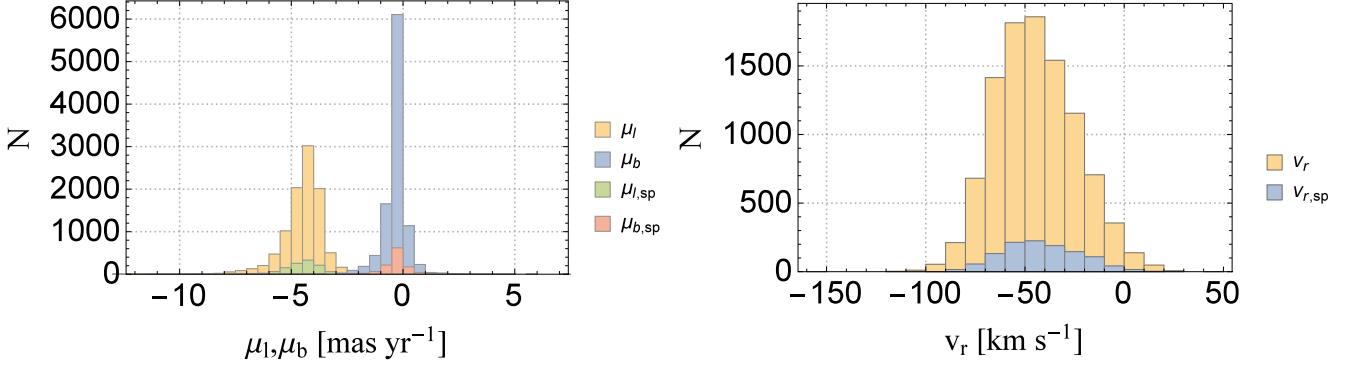
Figure 15. Proper motion distribution (left-hand panel) for a field of about 10 000 stars with spiral arms. The contribution of the spiral arms population is evidenced with subscript 'sp'. Right-hand panel: same as left-hand panel but for radial velocity. The CMD of this example is in Fig. 9.

obtains $\frac{\sigma_{zz}^2(R_\odot,z)}{\sigma_{zz}^2(R_\odot,0)} \simeq 1 + \frac{\lambda(R_\odot)}{2R_\odot}(\alpha - 1)|\frac{\partial \ln \sigma_{zz}^2}{\partial R}|_{(R_\odot,0)}z^2$. Supposing that $\sigma_{zz}^2 \propto \rho$ in the plane, as in van der Kruit & Searle (1982), and that ρ follows an exponential law with constant scalelength h_R we have $\frac{\sigma_{zz}^2(R_\odot,z)}{\sigma_{zz}^2(R_\odot,0)} \simeq 1 + \frac{\lambda(R_\odot)}{2R_\odot}(\frac{\sigma_{RR}^2(R_\odot,0)}{\sigma_{zz}^2(R_\odot,0)} - 1)\frac{z^2}{h_R}$ which describes the non-isothermal case as

$$\sigma_{zz}^2\left(R_\odot, z\right) \simeq \sigma_{zz}^2\left(R_\odot, 0\right)$$

$$+ \left(\frac{\lambda\left(R_\odot\right)}{2R_\odot}\left(\frac{\sigma_{RR}^2\left(R_\odot,0\right)}{\sigma_{zz}^2\left(R_\odot,0\right)} - 1\right)\frac{z^2}{h_R}\right)\sigma_{zz}^2\left(R_\odot,0\right), \quad (77)$$

or

$$\sigma_{zz}^2(R, z) \simeq \sigma_{zz}^2(R, 0) + \left.\frac{\lambda\left(\Phi\right)\left(\sigma_{RR}^2 - \sigma_{zz}^2\right)}{2 \cdot h_R \cdot R}\right|_{(R,0)} z^2, \quad (78)$$

which is clearly not constant. We have implemented this last formulation in our models to take the non-isothermal structure of the thin discs into account. This SSP non-isothermality based on Amendt & Cuddeford (1991) and Cuddeford & Amendt (1991) hydrodynamical model, applies to single stellar population (SSP) alone. However, it is observationally very difficult to identify a truly homogeneous population, i.e. in chemistry but also in age (e.g. Bovy et al. 2012a).

Finally, we can collect all this kinematic infrastructure to project it on the space of observations by plotting, e.g. the PDF of the proper motion $\mu_{l,b}$ and radial velocities v_r populated for the same field of Fig. 9 in Fig. 15.

8 COMPARISON WITH THE LITERATURE

Star count techniques have a long history and a comparison of all the different flavours of this approach is a complex task. Mainly two kinds of kinematical models and associated star counts are available in the literature. The first ones do not depend on the underlying gravitational potential. They contain a large number of constants treated as free parameters and therefore can quickly fit large samples of data simply because they do not integrate the Poisson equation. A prototype of this modelling approach is Ratnatunga, Bahcall & Casertano (1987, see e.g. Ratnatunga, Bahcall & Casertano 1989; Casertano, Ratnatunga & Bahcall 1990), who first applied the kinematical deconvolution of a DF in the phase space. Another model of this kind, with substantially no differences, is by Gilmore (1984). Mendez & van Altena (1996) and Méndez et al. (2000) further refined the star-counts approach to kinematical problems. Their work is based on the epicycle theory of disc kinematics and presents an original

treatment of the differential rotation based on the Jeans equations that allow studying of the asymmetric drift for each disc population. The limitation of these models is that the epicycle approximation limits the analysis of the disc kinematics only to regions near the plane and does not consider the vertical tilt of the velocity ellipsoid. Models of this kind, which are not based on a constrained potential may lead to somewhat non-physical solutions. Nevertheless, thanks to their simplification, they are useful to investigate more difficult problems which require formulations that are more sophisticated. For instance, the problem of the vertex deviation requires the axisymmetric hypothesis in the Poisson-solver to be relaxed. These difficulties are the subject of debate and strictly linked with the problems of modelling the bulge too.

The most popular global Galaxy model available in the literature and to which a finer comparison is due, is the Besançon model. This model has roots in the works by Robin & Creze (1986) and Bienaymé et al. (1987), later improved by Robin et al. (2003). This model not only simulates CMDs, taking into account all evolutionary phases of a star down to the white dwarf stages, but makes use of a kinematical description linked to the gravitational potential.

However, this model is not fully consistent from a dynamical point of view, equipped with much weaker dynamical constraints than what we are presenting here and missing a non-axisymmetric treatment of spiral arms. The method developed by Robin et al. (2003) is summarized in Bienaymé et al. (1987). Assuming suitable density profiles for the components of a galaxy, their method calculates the total density profile using the Poisson-solver in axisymmetric stationary conditions. The authors derive the gravitational potential from

$$\Delta\Phi_{tot}^{(I)}(R, z) = 4\pi G\rho_{tot}\left(R, z; \hat{R}_C^{(I)}, \hat{\rho}_C^{(I)}, \hat{M}_B^{(I)}, \hat{H}_{z,i}^{(I)}\right), \quad (79)$$

where $\{\hat{R}_C^{(I)}, \hat{\rho}_C^{(I)}, \hat{M}_B^{(I)}, \hat{H}_{z,i}^{(I)}\}$ are, respectively, the core radius of the halo, the central density of the disc, the total mass of the bulge, and the different scaleheights of the disc at their first (I) guess input. This equation yields the first guess of the potential $\Rightarrow \Phi_{tot}^{(I)}(R, z)$ where $\{\hat{R}_C^{(I)}, \hat{\rho}_C^{(I)}, \hat{M}_B^{(I)}\}$ have been considered as parameters. Obviously, some standard constraints are imposed such as the rotation curve $v_c^{(I)}(R) = R\partial_R\Phi_{tot}^{(I)}(R, z = 0)^{1/2}$ which can be compared with the observational data. The parameters are varied to match the rotation curve $v_{c,\text{bestfit}}(R) = R\partial_R\Phi_{tot}^{(I)}(R, z = 0; R_C^{(II)}, \rho_C^{(II)}, M_B^{(II)}, \hat{H}_{z,i}^{(I)})^{1/2}$ and the new parameters $\{\hat{R}_C^{(II)}, \hat{\rho}_C^{(II)}, \hat{M}_B^{(II)}\}$ are used to obtain a second guess for the potential $\Delta\Phi_{tot}^{(II)}(R, z) = 4\pi G\rho_{tot}(R, z; \hat{R}_C^{(II)}, \hat{\rho}_C^{(II)}, \hat{M}_B^{(II)}, \hat{H}_{z,i}^{(I)})$ satisfying the first dynamical constraint set by the rotation curve. The model seeks then

to satisfy the Boltzmann equation. Using the Jeans equation their model assumes, in contrast with our model, that $\sigma_{Rz} = \overline{(v_R - \bar{v}_R)(v_z - \bar{v}_z)} = \overline{v_R v_z} = 0$ i.e. $\frac{\partial \rho \overline{v_R v_z}}{\partial R} - \frac{\rho \overline{v_R v_z}}{R} = 0$. With this simplification, the Jeans equation reduces to $\frac{\partial \rho \overline{v_z^2}}{\partial z} + \rho \frac{\partial \Phi_{tot}}{\partial z} = 0$ and assuming isothermal behaviour $\sigma_{zz}^2 \frac{\partial \rho}{\partial z} + \rho \frac{\partial \Phi_{tot}}{\partial z} = 0$, where $\sigma_{zz}^2 = \overline{(v_z - \bar{v}_z)^2} = \overline{v_z^2}$. This equation can immediately be solved $\Phi_{tot}(R, z) = c_1 - \sigma_{zz}^2 \ln(\rho(R, z))$. This means that another solution of this equation is $\Phi_{tot}(R, z = 0) = c_1 - \sigma_{zz}^2 \ln(\rho(R, z = 0))$. Subtracting the two solutions, we obtain another solution and the implemented equation $\sigma_{zz}^2 \ln(\frac{\rho(R,z)}{\rho(R,0)}) = -\Phi_{tot}(R, z) + \Phi_{tot}(R, 0)$, that is already present in Mihalas & Routly ([1968]). The model makes use of this equation to obtain the best fit of the disc scalelength with an iterative procedure. The dynamical consistency is clearly poorer than that in our kinematical model, where formulation for the mixed terms $\sigma_{R\phi} = \sigma_{R\phi}(\Phi_{tot})$ and $\sigma_{Rz} = \sigma_{Rz}(\Phi_{tot})$ are both obtained with consistency from the potential as well as the non-isothermality of $\sigma_{zz}(z)$. This helps to decrease the large number of parameters, thus strengthening the consistency of our model. Our approximation implicitly assumes a kinematically cold disc. Moreover, in the case of the Galactic potential no analytical, realistic formulation of the third integral of motion (which is likely responsible for the small irregularities present in the Galaxy structure) is available. Therefore, it is not yet analytically possible to derive a correct DF that, thanks to the Jeans' Theorem, could satisfy the self-consistency requirements. A hypothesis in common to our kinematical model and the one by Robin et al. ([2003]) is the stationary state of the DF. The trishifted Gaussian represents the only analytical solution of the Boltzmann equation in a steady state and it is commonly adopted in several models.

As it is not easy to satisfy the dynamical consistency, many kinematical models are possible and their solution is degenerate. Based on these considerations, instead of the iterative procedure adopted in Robin et al. ([2003]) for which no unique solution is guaranteed, it is perhaps better to let all parameters remain free to converge to the best-fitting solution with no ad hoc limits. Clearly, the best way to proceed is to simultaneously constrain as many parameters as possible with the suitable minimization algorithms that we described in Section 5.

Finally, we point out how in our model, the Poisson solver is exactly the same as in Robin et al. ([2003]), but our analytical treatment allows us to consider the coupled potential along the vertical-radial direction. This is not possible with the Robin et al. ([2003]) model that neither follows the vertical variation of the vertical tilt of the velocity ellipsoid nor the variations of the velocity ellipsoid vertical axis with the stellar populations nor the radial velocity coupling with the presence of spiral arms. Both the Robin et al. ([2003]) and our models allow for a gradient in the vertical component of the temperature profiles, i.e. $\sigma_{zz}^2(R) = \sum_{i=1}^{n} \sigma_{zz,i}^2$. However, in the Robin et al. ([2003]) model all the $\sigma_{zz,i}^2$ are considered constant for all stellar populations, i.e. $\sigma_{zz,i}^2 = \text{const}. \forall i$. Therefore, the temperature gradient is a consequence of the different scaleheight of each population. In contrast, each stellar population in our model has its own vertical profile, i.e. $\sigma_{zz,i}^2 = \sigma_{zz,i}^2(R) \forall i$. This makes it possible to examine separately different types of SSP. The task is nowadays feasible thanks to the wealth of data and even more in the near future with *Gaia*, whose data will probably give definitive answers to long lasting problems such as the vertical isothermality, presence of DM and the origin of the Galactic discs.

Our model has the significant advantage of reproducing several observational constraints, such as (Section 4) the rotation curve, the outer rotation curve, the Oort functions and constants, the mass inside 100 kpc, the vertical force, the surface density, and the parameter λ in the solar neighbourhood.

Clearly, the space of parameter dimensions grows with the square of the number of parameters; however, the number of important parameters is rather small. The interplay between a gravitational potential satisfying all the constraints and parameter adjustment to fit the observational CMDs secures the kinematical consistency of the model, as the kinematics are simultaneously derived from the potential and the properties of the stellar populations generating the potential. One has to remember that the DF has different dispersion axes for each population and that the angular momentum for the orbits is linked to the rotational velocity via the Boltzmann equation moments.

9 CONCLUSIONS

We presented a Galaxy model which can be used to investigate large data sets focused from MW surveys in great detail, of the Milky Way with particular attention to the kinematical modelling. This model gathered the heritage of the Padua model that stems from the early studies of the stellar content of the Palomar–Groeningen survey towards the Galactic Centre by Ng et al. ([1995]) and Bertelli et al. ([1995]), followed by studies of specific groups of stars and interstellar extinction by Bertelli et al. ([1995], [1996]), Ng & Schultheis ([1997]) and Ng & Bertelli ([1996]) to mention a few, the studies of the stellar content towards the Galactic Pole (Ng et al. [1997]), the development of a new minimization technique for the diagnostics of stellar population synthesis (Ng [1998a]), the study of the Galactic Disc Age–Metallicity relation (Carraro, Ng & Portinari [1998]), the possible relationship between the bulge C-stars and the Sagittarius dwarf galaxy (Ng [1998b]), the developments of AMORE (Automatic Observation Rendering) of a synthetic stellar population's CMD based on the genetic algorithm (Ng et al. [2002]), the study of 3D structure of the Galaxy from star-counts in view of the *Gaia* mission (Vallenari et al. [2003]) and of the kinematics of the Galactic populations towards the North Pole with mock *Gaia* data (Vallenari et al. [2004], [2006]; Pasetto [2005]).

The building blocks of the Padua Galactic model are a synthetic Hertzsprung–Russell diagram generator a kinematical model, and an MW gravitational potential model. This tool has now been updated following a novel approach to the theory of population synthesis that borrows and adapts to the present aims a few concepts from statistical mechanics.

(i) The model is grounded on the concept of the PDF for stellar populations. The system-Galaxy is framed in a theoretical existence space where it is characterized by a number of key relations (mass function, age–metallicity, phase-space, and metallicity/phase-space).

(ii) The model is able to analyse and reproduce observable quantities regardless of size and amounts of the data to a analyse: this is achieved thanks to the use of PDF instead of star-counts.

(iii) The distribution of mass and mass density and associated gravitational potential are thoroughly discussed and formulated for each component of the MW together with a few other important issues such as the rotation curve, the vertical force acting on the plane, the presence of spiral arms and their effects on dynamics and kinematics, the presence of non-axisymmetric features etc.

(iv) Particular effort is paid to include spiral arms for which we develop a completely new treatment of the mass density, kinematics and extinction. Several treatments of the resonance areas to deal with the star-count technique have been explored and implemented.

(v) A novel formulation for the extinction has been implemented to account for the new non-axisymmetric features of the model and in preparation for a forthcoming star-count model of the bulge.

(vi) A genetic algorithm has been included to deal simultaneously with photometric information, as well as kinematical and gravitational information.

(vii) Particular care is paid to the photometric population synthesis to simulate the photometric properties, magnitudes and colours for samples of stars of unprecedented size taking advantage of the concept of PDF to populate CMDs and luminosity functions bearing in mind the data that will soon be acquired by space observatories like *Gaia*.

(viii) The model has been compared with similar models in literature, for instance the popular Besançon model, to highlight differences and similarities.

The range of applicability of our Galaxy model is very large. It can already be applied to existing MW surveys on which the model has already been tested. None of the existing surveys are actually comparable with *Gaia* for precision and amounts of data, but all of them already investigate different aspects of the Galaxy. To mention a few, we recall the Radial Velocity Experiment (Steinmetz et al. 2006; Zwitter et al. 2008; Siebert et al. 2011) of which the fourth data release (Kordopatis et al. 2013) has been used to test the model (Pasetto et al. 2012c,d). The Galaxy model could be applied to the data coming from the Apache Point Observatory Galactic Evolution Experiment (e.g. Majewski et al. 2015), a companion programme of the Sloan Digital Sky Survey (Ahn et al. 2014) that makes available an infrared catalogue of several hundred thousands radial velocities (from high-resolution spectra) that are suitable to stellar population studies within the plane. This data base is especially interesting when used in combination with the data from the Kepler/K2 mission, because this would allow us to investigate stellar populations also with photometry. The ongoing GALAH survey (De Silva et al. 2015), a large Australian project that will measure the abundances of 30 elements together with HERMES providing spectrographic measurements of radial velocities is another example to which the Galaxy model could be applied to investigate the galactic archaeology and archeochemistry.

Finally, our model can be applied also to entirely different astrophysical scales, such as in asteroseismology. When spectroscopic analysis is combined with seismic information, precise constraints on distances, masses, extinction and finally ages can be obtained. The *CoRoT* red giant field (e.g. Chiappini et al. 2015) analysis is an example, even though the statistical samples are still very small.

A golden age for systematic studies of MW is imminent. Existing photometric and spectroscopic surveys, as well as future ones such as *Gaia*, will be crucial to obtain the ultimate model of our own Galaxy, a fundamental local step to interpret the Universe in a cosmological framework. In this context, the Galaxy model we have developed is awaiting complete validation by more precise kinematical data, ages and metallicities. In the meantime, we have presented here the first kinematical model that can simultaneously deal with the age–velocity and dispersion–metallicity relations in a robust dynamical-kinematical framework over the whole space of variables defined by the proper motions, radial velocities, and multiband photometric data (magnitudes and colours). Future developments will include an upgrading of the bulge to include non-axisymmetric descriptions of the bar and chemical enrichment.

The Galaxy model can be access from the internet interface at www.galmod.org and questions addressed at the email: galaxy.model@yahoo.com.

REFERENCES

Abramowitz M., Stegun I. A., 1972, Handbook of Mathematical Functions. Dover Press, New York

Ahn C. P. et al., 2014, ApJS, 211, 17

Allard F., Hauschildt P. H., Alexander D. R., Ferguson J. W., Tamanai A., 2000, in Griffith C. A., Marley M. S., eds, ASP Conf. Ser. Vol. 212, From Giant Planets to Cool Stars. Astron. Soc. Pac., San Francisco, p. 127

Alongi M., Bertelli G., Bressan A., Chiosi C., 1991, A&A, 244, 95

Alongi M., Bertelli G., Bressan A., Chiosi C., Fagotto F., Greggio L., Nasi E., 1993, A&AS, 97, 851

Amendt P., Cuddeford P., 1991, ApJ, 368, 79

Andrievsky S. M., Luck R. E., Martin P., Lépine J. R. D., 2004, A&A, 413, 159

Aparicio A., Gallart C., 1995, AJ, 110, 2105

Aparicio A., Gallart C., Chiosi C., Bertelli G., 1996, ApJ, 469, L97

Arnold R., 1995, MNRAS, 276, 293

Bahcall J. N., 1984a, BAAS, 16, 733

Bahcall J. N., 1984b, ApJ, 287, 926

Bahcall J. N., Soneira R. M., 1984, ApJS, 55, 67

Barnes J., Hut P., 1986, Nature, 324, 446

Barros D. A., Lépine J. R. D., Junqueira T. C., 2013, MNRAS, 435, 2299

Bassino L. P., Dessaunet V. H., Muzzio J. C., 1986, Rev. Mex. Astron. Astrofis., 13, 9

Belokurov V. et al., 2006, ApJ, 642, L137

Bergemann M., Ruchti G. R., Serenelli A., Feltzing S., Alves-Brito A., Asplund M., Bensby T., 2014, A&A, 565, A89

Bertelli G., Nasi E., 2001, AJ, 121, 1013

Bertelli G., Bressan A., Chiosi C., Fagotto F., Nasi E., 1994, A&AS, 106, 275

Bertelli G., Bressan A., Chiosi C., Ng Y. K., Ortolani S., 1995, A&A, 301, 381

Bertelli G., Bressan A., Chiosi C., Ng Y. K., 1996, A&A, 310, 115

Bertelli G., Nasi E., Girardi L., Chiosi C., Zoccali M., Gallart C., 2003, AJ, 125, 770

Bertelli G., Girardi L., Marigo P., Nasi E., 2008, A&A, 484, 815

Bertelli G., Nasi E., Girardi L., Marigo P., 2009, A&A, 508, 355

Bertin G., 2014, Dynamics of Galaxies. Cambridge Univ. Press, Cambridge

Bessell M. S., 1990, PASP, 102, 1181

Bessell M. S., Brett J. M., 1988, PASP, 100, 1134

Bhattacharjee P., Chaudhury S., Kundu S., 2014, ApJ, 785, 63

Bienaymé O., 1999, A&A, 341, 86

Bienaymé O., 2000, in Schielicke R. E., ed., Astronomische Gesellschaft Meeting Abstracts, Vol. 16, Dynamics of Star Clusters and the Milky Way. Astron. Soc. Pac., San Francisco, p. 10

Bienaymé O., 2009, A&A, 500, 781

Bienaymé O., Traven G., 2013, A&A, 549, A89

Bienayme O., Robin A. C., Creze M., 1987, A&A, 180, 94

Bienaymé O., Soubiran C., Mishenina T. V., Kovtyukh V. V., Siebert A., 2006, A&A, 446, 933

Bienaymé O. et al., 2014, A&A, 571, A92

Bienaymé O., Robin A. C., Famaey B., 2015, A&A, 581, A123

Boeche C. et al., 2013, A&A, 559, A59

Boeche C., Siebert A., Piffl T., Just A., Steinmetz M., Grebel E. K., Sharma S., Kordopatis G., 2014, A&A, 568, A71

Bovy J., Rix H.-W., Liu C., Hogg D. W., Beers T. C., Lee Y. S., 2012a, ApJ, 753, 148

Bovy J., Rix H.-W., Hogg D. W., Beers T. C., Lee Y. S., Zhang L., 2012b, ApJ, 755, 115

Bratek Ł., Sikora S., Jałocha J., Kutschera M., 2014, A&A, 562, A134

Bressan A. G., Chiosi C., Bertelli G., 1981, A&A, 102, 25

Brosche P., Schwan H., 1981, A&A, 99, 311

Byl J., Ovenden M. W., 1981, MNRAS, 196, 659

Carlberg R. G., Innanen K. A., 1987, AJ, 94, 666

Carraro G., Ng Y. K., Portinari L., 1998, MNRAS, 296, 1045

Casertano S., Ratnatunga K. U., Bahcall J. N., 1990, ApJ, 357, 435

Castelli F., Kurucz R. L., 2003, in Piskunov N., Weiss W. W., Gray D. F., eds, Proc. IAU Symp. 210, Modelling of Stellar Atmospheres. Kluwer, Dordrecht, p. 210

Chabrier G., 2003, PASP, 115, 763

Charbonneau P., 1995, ApJS, 101, 309

Chemin L., Renaud F., Soubiran C., 2015, A&A, 578, A14

Chen B. et al., 2001, ApJ, 553, 184

Chiappini C., Anders F., Rodrigues T. S., Miglio A., Montalbán J., Mosser B., Girardi L., Valentini M., 2015, A&A, 576, L12

Chiosi C., 1980, A&A, 83, 206

Chiosi C., Greggio I., 1981, A&A, 98, 336

Chiosi C., Summa C., 1970, Ap&SS, 8, 478

Chiosi C., Bertelli G., Bressan A., Nasi E., Pigatto L., 1986, in Kunth D., Thuan T. X., Tran Thanh Van J., Lequeux J., Audouze J., eds, Star-Forming Dwarf Galaxies and Related Objects. p. 449

Chiosi C., Bertelli G., Meylan G., Ortolani S., 1989, A&A, 219, 167

Comeron F., Torra J., 1991, A&A, 241, 57

Creze M., Mennessier M. O., 1973, A&A, 27, 281

Cubarsi R., 2007, MNRAS, 380, 848

Cubarsi R., 2014a, A&A, 561, A141

Cubarsi R., 2014b, A&A, 567, A46

Cuddeford P., Amendt P., 1991, MNRAS, 253, 427

Cuddeford P., Amendt P., 1992, MNRAS, 256, 166

Curir A., Serra A. L., Spagna A., Lattanzi M. G., Re Fiorentin P., Diaferio A., 2014, ApJ, 784, L24

D'Onghia E., Vogelsberger M., Hernquist L., 2013, ApJ, 766, 34

De Silva G. M. et al., 2015, MNRAS, 449, 2604

De Simone R., Wu X., Tremaine S., 2004, MNRAS, 350, 627

Deason A. J., Belokurov V., Evans N. W., 2011, MNRAS, 411, 1480

Deason A. J., Belokurov V., Evans N. W., An J., 2012, MNRAS, 424, L44

Debattista V. P., Roškar R., Valluri M., Quinn T., Moore B., Wadsley J., 2013, MNRAS, 434, 2971

Dehnen W., 1998, AJ, 115, 2384

Dehnen W., 1999a, AJ, 118, 1190

Dehnen W., 1999b, ApJ, 524, L35

Dehnen W., Binney J., 1998, MNRAS, 294, 429

Dejonghe H., de Zeeuw T., 1988, ApJ, 333, 90

Dejonghe H., Laurent D., 1991, MNRAS, 252, 606

Dékány I. et al., 2015, ApJ, 812, L29

Deng L., Bressan A., Chiosi C., 1996a, A&A, 313, 145

Deng L., Bressan A., Chiosi C., 1996b, A&A, 313, 159

Draine B. T., Li A., 2007, ApJ, 657, 810

Eddington A. S., 1915, MNRAS, 76, 37

Erdélyi A., Magnus W., Oberhettinger F., Tricomi F., 1954, Tables Of Integral Transforms I and II. McGraw-Hill, New York

Evans N. W., de Zeeuw P. T., 1992, MNRAS, 257, 152

Evans N. W., de Zeeuw P. T., Lynden-Bell D., 1990, MNRAS, 244, 111

Fagotto F., Bressan A., Bertelli G., Chiosi C., 1994a, A&AS, 105, 29

Fagotto F., Bressan A., Bertelli G., Chiosi C., 1994b, A&AS, 105, 39

Famaey B., Dejonghe H., 2003, MNRAS, 340, 752

Faure C., Siebert A., Famaey B., 2014, MNRAS, 440, 2564

Feast M., Whitelock P., 1997a, MNRAS, 291, 683

Feast M. W., Whitelock P. A., 1997b, in Bonnet R. M. et al., eds, ESA SP-402: Hipparcos - Venice '97'. ESA, Noordwijk, p. 625

Feitzinger J. V., Spicker J., 1986, PASJ, 38, 485

Fermani F., Schönrich R., 2013, MNRAS, 432, 2402

Fernández D., Figueras F., Torra J., 2001, A&A, 372, 833

Fitzpatrick E. L., 1999, PASP, 111, 63

Fluks M. A., Plez B., The P. S., de Winter D., Westerlund B. E., Steenman H. C., 1994, A&AS, 105, 311

Fuchs B., Wielen R., 1987, in Gilmore G., Carswell B., eds, The Galaxy. Reidel, Dordrecht, p. 375

García-Sánchez J., Weissman P. R., Preston R. A., Jones D. L., Lestrade J.-F., Latham D. W., Stefanik R. P., Paredes J. M., 2001, A&A, 379, 634

Gerhard O., 2002, Space Sci. Rev., 100, 129

Ghosh P., Bhattacharjee P., Cowsik R., 1989, ApJ, 345, 647

Gilmore G., 1984, MNRAS, 207, 223

Gilmore G., Wyse R. F. G., Norris J. E., 2002, ApJ, 574, L39

Gilmore G. et al., 2012, The Messenger, 147, 25

Girardi L., Bertelli G., Bressan A., Chiosi C., Groenewegen M. A. T., Marigo P., Salasnich B., Weiss A., 2002, A&A, 391, 195

Girardi L., Groenewegen M. A. T., Hatziminaoglou E., da Costa L., 2005, A&A, 436, 895

Girardi L., Castelli F., Bertelli G., Nasi E., 2007, A&A, 468, 657

Golubov O., Just A., 2013, in Wong T., Ott J., eds, Proc. IAU Symp. 292, The Density Model of the Milky Way from the Tangent-Point Measurements of the Rotation Curve. Cambridge Univ. Press, Cambridge, p. 101

Grand R. J. J., Kawata D., Cropper M., 2012a, MNRAS, 421, 1529

Grand R. J. J., Kawata D., Cropper M., 2012b, MNRAS, 426, 167

Greggio L., Renzini A., 2011, Stellar Populations. A User Guide from Low to High Redshift. Wiley, New York

Griv E., Ngeow C.-C., Jiang I.-G., 2013, MNRAS, 433, 2511

Griv E., Lin C.-C., Ngeow C.-C., Jiang I.-G., 2014, New Astron., 29, 9

Hanson R. B., 1987, AJ, 94, 409

Haywood M., Robin A. C., Creze M., 1997, A&A, 320, 428

Helmi A., White S. D. M., Springel V., 2003, MNRAS, 339, 834

Hernquist L., 1990, ApJ, 356, 359

Hill G., Hilditch R. W., Barnes J. V., 1979, MNRAS, 186, 813

Hilton J. L., Bash F., 1982, ApJ, 255, 217

Holland J. H., 1975, Adaptation in Natural and Artificial Systems. an Introductory Analysis with Applications to Biology, Control and Artificial Intelligence. University of Michigan Press, Ann Arbor

Huang Y. et al., 2016, preprint (arXiv:1604.01216)

Hunt J. A. S., Kawata D., 2013, MNRAS, 430, 1928

Hunt J. A. S., Kawata D., Grand R. J. J., Minchev I., Pasetto S., Cropper M., 2015, MNRAS, 450, 2132

Hunter C., de Zeeuw P. T., Park C., Schwarzschild M., 1990, ApJ, 363, 367

Jałocha J., Sikora S., Bratek Ł., Kutschera M., 2014, A&A, 566, A87

Junqueira T. C., Lépine J. R. D., Braga C. A. S., Barros D. A., 2013, A&A, 550, A91

Just A., Jahreiß H., 2010, MNRAS, 402, 461

Just A., Gao S., Vidrih S., 2011, MNRAS, 411, 2586

Kafle P. R., Sharma S., Lewis G. F., Bland-Hawthorn J., 2014, ApJ, 794, 59

Kawata D., Hunt J. A. S., Grand R. J. J., Pasetto S., Cropper M., 2014, MNRAS, 443, 2757

Kerr F. J., Lynden-Bell D., 1986, MNRAS, 221, 1023

Klypin A., Zhao H., Somerville R. S., 2002, ApJ, 573, 597

Kordopatis G. et al., 2013, AJ, 146, 134

Kroupa P., 2001, MNRAS, 322, 231

Kroupa P., Tout C. A., Gilmore G., 1993, MNRAS, 262, 545

Kuijken K., Gilmore G., 1989a, MNRAS, 239, 571

Kuijken K., Gilmore G., 1989b, MNRAS, 239, 605

Kuijken K., Gilmore G., 1989c, MNRAS, 239, 651

Leaman R., VandenBerg D. A., Mendel J. T., 2013, MNRAS, 436, 122

Lépine J. R. D., Mishurov Y. N., Dedikov S. Y., 2001, ApJ, 546, 234

Lépine J. R. D., Acharova I. A., Mishurov Y. N., 2003, ApJ, 589, 210

Levine E. S., Heiles C., Blitz L., 2008, ApJ, 679, 1288

Lewis J. R., Freeman K. C., 1989, AJ, 97, 139

Licquia T., Newman J., 2013, BAAS, 221, 254.11

Licquia T. C., Newman J. A., 2015, ApJ, 806, 96

Lin C. C., Shu F. H., 1964, ApJ, 140, 646

Lin C. C., Yuan C., Shu F. H., 1969, ApJ, 155, 721

Lindblad B., 1958, Ric. Astron., 5, 467

Loidl R., Lançon A., Jørgensen U. G., 2001, A&A, 371, 1065

López-Corredoira M., 2014, A&A, 563, A128

McMillan P. J., 2011, MNRAS, 414, 2446

Majewski S. R., Schiavon R. P., Frinchaboy P. M., Allende Prieto C., Barkhouser R., Bizyaev D., Blank B., 2015, preprint (arXiv:e-prints)

Marigo P., Girardi L., 2007, A&A, 469, 239

Marochnik L. S., 1964, Sov. Astron., 8, 202

Marochnik L. S., 1966, Sov. Astron., 10, 442

Marochnik L. S., 1967, Sov. Astron., 10, 738

Marochnik L. S., Ptitsina N. G., 1968, Sov. Astron., 12, 411

Marochnik L. S., Suchkov A. A., 1969a, Sov. Astron., 13, 252

Marochnik L. S., Suchkov A. A., 1969b, Sov. Astron., 13, 411

Mathieu A., Dejonghe H., 1996, A&A, 314, 25

Mayor M., 1972, A&A, 18, 97

Mendez R. A., van Altena W. F., 1996, AJ, 112, 655

Méndez R. A., Platais I., Girard T. M., Kozhurina-Platais V., van Altena W. F., 2000, AJ, 119, 813

Merritt D., Stiavelli M., 1990, ApJ, 358, 399

Metcalfe T. S., Charbonneau P., 2003, J. Comput. Phys., 185, 176

Mihalas D., Routly P. M., 1968, Galactic Astronomy. Freeman & Co., San Francisco

Minchev I., Quillen A. C., 2007, MNRAS, 377, 1163

Mishurov Y. N., Zenina I. A., 1999, A&A, 341, 81

Mishurov Y. N., Zenina I. A., Dambis A. K., Mel'Nik A. M., Rastorguev A. S., 1997, A&A, 323, 775

Nelson A. H., Matsuda T., 1977, MNRAS, 179, 663

Ng Y. K., 1998b, A&A, 338, 435

Ng Y. K., 1998a, A&AS, 132, 133

Ng Y. K., Bertelli G., 1996, A&A, 315, 116

Ng Y. K., Schultheis M., 1997, A&AS, 123, 115

Ng Y. K., Bertelli G., Bressan A., Chiosi C., Lub J., 1995, A&A, 295, 655

Ng Y. K., Bertelli G., Chiosi C., Bressan A., 1997, A&A, 324, 65

Ng Y. K., Brogt E., Chiosi C., Bertelli G., 2002, A&A, 392, 1129

Olling R. P., Dehnen W., 2003, ApJ, 599, 275

Olling R. P., Merrifield M. R., 1998, MNRAS, 297, 943

Olling R. P., Merrifield M. R., 2001, MNRAS, 326, 164

Osipkov L. P., 1994, Astron. Lett., 20, 429

Pasetto S., 2005, PhD thesis, Univ. Edinburgh

Pasetto S., Bertelli G., Grebel E. K., Chiosi C., Fujita Y., 2012a, A&A, 542, A17

Pasetto S., Chiosi C., Kawata D., 2012b, A&A, 545, A14

Pasetto S. et al., 2012c, A&A, 547, A70

Pasetto S. et al., 2012d, A&A, 547, A71

Pietrinferni A., Cassisi S., Salaris M., Castelli F., 2006, ApJ, 642, 797

Pilyugin L. S., Edmunds M. G., 1996, A&A, 313, 792

Pohlen M., Trujillo I., 2006, A&A, 454, 759

Quillen A. C., Minchev I., 2005, AJ, 130, 576

Ratnatunga K. U., Bahcall J. N., Casertano S., 1987, BAAS, 19, 679

Ratnatunga K. U., Bahcall J. N., Casertano S., 1989, ApJ, 339, 106

Robin A., Creze M., 1986, A&A, 157, 71

Robin A. C., Reylé C., Derrière S., Picaud S., 2003, A&A, 409, 523

Roca-Fàbrega S., Antoja T., Figueras F., Valenzuela O., Romero-Gómez M., Pichardo B., 2014, MNRAS, 440, 1950

Rocha-Pinto H. J., Maciel W. J., Scalo J., Flynn C., 2000, A&A, 358, 850

Rocha-Pinto H. J., Flynn C., Scalo J., Hänninen J., Maciel W. J., Hensler G., 2004, A&A, 423, 517

Rocha-Pinto H. J., Rangel R. H. O., Porto de Mello G. F., Bragança G. A., Maciel W. J., 2006, A&A, 453, L9

Roškar R., Debattista V. P., Quinn T. R., Wadsley J., 2012, MNRAS, 426, 2089

Sackett P. D., Sparke L. S., 1990, ApJ, 361, 408

Salaris M., Cassisi S., 2005, Evolution of Stars and Stellar Populations. Wiley, New York

Salasnich B., Bressan A., Chiosi C., 1999, A&A, 342, 131

Salpeter E. E., 1955, ApJ, 121, 161

Seabroke G. M., Gilmore G., 2007, MNRAS, 380, 1348

Sellwood J. A., Carlberg R. G., 2014, ApJ, 785, 137

Shu F., 1991, Physics of Astrophysics, Vol. I. University Science Books, Mill Valley, CA

Siebert A., Bienaymé O., Soubiran C., 2003, A&A, 399, 531

Siebert A. et al., 2011, AJ, 141, 187

Smith M. C., Ruchti G. R., Helmi A., Wyse R. F. G., Fulbright J. P., Freeman K. C., Navarro J. F., Seabroke G. M., 2007, MNRAS, 379, 755

Soubiran C., Bienaymé O., Siebert A., 2003, A&A, 398, 141

Soubiran C., Bienaymé O., Mishenina T. V., Kovtyukh V. V., 2008, A&A, 480, 91

Steinmetz M. et al., 2006, AJ, 132, 1645

Stetson P. B., Harris W. E., 1988, AJ, 96, 909

Trumpler R. J., Weaver H. F., 1953, Statistical Astronomy. Dover Press, New York

Vallée J. P., 2014, MNRAS, 442, 2993

Vallée J. P., 2016a, AJ, 151, 55

Vallée J. P., 2016b, ApJ, 821, 53

Vallenari A., Bertelli G., Chiosi C., Nasi E., Pasetto S., Carraro G., 2003, Mem. Soc. Astron. Ital., 74, 522

Vallenari A., Pasetto S., Bertelli G., Chiosi C., Ragaini S., Spagna A., 2004, in Clemens D., Shah R., Brainerd T., eds, ASP Conf. Ser. Vol. 317, Milky Way Surveys: The Structure and Evolution of our Galaxy. Astron. Soc. Pac., San Francisco, p. 203

Vallenari A., Pasetto S., Bertelli G., Chiosi C., Spagna A., Lattanzi M., 2006, A&A, 451, 125

van de Ven G., Hunter C., Verolme E. K., de Zeeuw P. T., 2003, MNRAS, 342, 1056

van der Kruit P. C., 1988, A&A, 192, 117

van der Kruit P. C., Freeman K. C., 1986, ApJ, 303, 556

van der Kruit P. C., Searle L., 1982, A&A, 110, 61

Verolme E. K., de Zeeuw P. T., 2002, MNRAS, 331, 959

Wada K., Baba J., Saitoh T. R., 2011, ApJ, 735, 1

Wainscoat R. J., Freeman K. C., Hyland A. R., 1989, ApJ, 337, 163

Widrow L. M., Pym B., Dubinski J., 2008, ApJ, 679, 1239

Widrow L. M., Gardner S., Yanny B., Dodelson S., Chen H.-Y., 2012, ApJ, 750, L41

Wilkinson M. I., Evans N. W., 1999, MNRAS, 310, 645

Williams M. E. K., Steinmetz M., Binney J., Siebert A., Enke H., 2013, MNRAS, 436, 101

Woolley R., 1970, in Becker W., Kontopoulos G. I., eds, Proc. IAU Symp. 38, The Spiral Structure of our Galaxy. Reidel, Dordrecht, p. 423

Xin X.-S., Zheng X.-W., 2013, Res. Astron. Astrophys., 13, 849

Xue X. X. et al., 2008, ApJ, 684, 1143

Yoon J. H., Johnston K. V., Hogg D. W., 2011, ApJ, 731, 58

Zwitter T. et al., 2008, AJ, 136, 421

APPENDIX A: HYPERGEOMETRIC FORMULATION OF THE 'REDUCTION FACTOR'

There is quite a number of works in the literature, see section 1, that based the interpretation of the reduction factor on the work of Lin et al. (1969) through the computation of the 'q'-factor, i.e. the integral of equation B8 in appendix B of the mentioned paper. In this appendix, we express for the first time that integral as a function of the well-known hypergeometric function. To achieve this result, we make use of the following theorem.

Theorem: from Erdlyi et al. (1954, Vol 2, pg. 400, equation 8), we have that for any $\{z, \alpha, \beta, \gamma, \delta\} \in \mathbb{C}$ with $\mathrm{Re}\gamma > 0$, $\mathrm{Re}\rho > 0$ and $\mathrm{Re}(\gamma + \rho - \alpha - \beta) > 0$ the following relation holds:

$$
{}_2F_2(\rho, \gamma + \rho - \alpha - \beta; \gamma + \rho - \alpha, \gamma + \rho - \beta; z)
$$

$$
= \frac{\Gamma(\gamma + \rho - \alpha)\,\Gamma(\gamma + \rho - \beta)}{\Gamma(\gamma)\,\Gamma(\rho)\,\Gamma(\gamma + \rho - \alpha - \beta)}\, \mathrm{e}^z
$$

$$
\times \int_0^1 x^{\gamma - 1}(1 - x)^{\rho - 1} \mathrm{e}^{-xz}\, {}_2F_1(\alpha, \beta; \gamma; x)\, \mathrm{d}x, \tag{A1}
$$

with ${}_2F_2(*)$ the hypergeometric function and Γ the Eulero-gamma function.

We want to prove the following corollary to the previous theorem.

Corollary. For any $\{z, \nu\} \in \mathbb{R}$, the following relation holds:

$$\frac{1}{2\pi} \int_{-\pi}^{\pi} \cos(\nu s) e^{-z(\cos(s)+1)} ds = {}_2\tilde{F}_2\left(\frac{1}{2}, 1; 1 - \nu, \nu + 1; -2z\right),$$

(A2)

where ${}_2\tilde{F}_2$ is the hypergeometric-regularized function.

Proof. We start relating the hypergeometric-regularized function, ${}_2\tilde{F}_2$, to the hypergeometric function, ${}_2F_2$, by writing

$${}_2\tilde{F}_2\left(\frac{1}{2}, 1; 1 - \nu, \nu + 1; -2z\right)$$

$$= \frac{\sin(\pi\nu)}{\pi\nu} \, {}_2F_2\left(\frac{1}{2}, 1; 1 - \nu, \nu + 1; -2z\right).$$

(A3)

This equation, because of the theorem equation (A1) reduces to

$$\frac{\sin(\pi\nu)}{\pi\nu} \, {}_2F_2\left(\frac{1}{2}, 1; 1 - \nu, \nu + 1; -2z\right)$$

$$= \frac{\sin(\pi\nu)}{\pi\nu} \frac{\Gamma(1-\nu)\Gamma(\nu+1)}{\pi} e^{-2z} \int_0^1 \frac{e^{2xz} \, {}_2F_1\left(\nu, -\nu; \frac{1}{2}; x\right)}{\sqrt{1-x}\sqrt{x}} dx$$

$$= \frac{1}{\pi} \frac{\sin(\pi\nu)}{\nu} \frac{\nu}{\sin(\pi\nu)} e^{-2z} \int_0^1 \frac{e^{2xz} \cos\left(2\nu \arcsin\sqrt{x}\right)}{\sqrt{1-x}\sqrt{x}} dx$$

$$= \frac{e^{-2z}}{\pi} \int_0^1 \frac{2e^{2y^2z} \cos\left(2\nu \arcsin y\right)}{\sqrt{1-y^2}} dy$$

$$= \frac{e^{-2z}}{\pi} \int_0^{\pi/2} 2e^{2z\sin^2 q} \cos\left(2q\nu\right) dq,$$

(A4)

where in the second line we made use of ${}_2F_1$ and Eulero-gamma function properties, in the third and fourth rows we change variables, $x = y^2$ and $y = \sin q$, accounting for the dominion of integration. The last relation is clearly an even function, thus

$${}_2\tilde{F}_2\left(\frac{1}{2}, 1; 1 - \nu, \nu + 1; -2z\right) = \frac{1}{\pi} \int_0^\pi e^{-2z+2z\sin^2 s/2} \cos\left(\nu s\right) ds$$

$$= \frac{1}{2\pi} \int_{-\pi}^{\pi} e^{-z(1+\cos s)} \cos(\nu s) ds,$$

(A5)

which concludes our proof. The expression for the reduction factor comes then easily.

Needless to say that the advantage of having this formulation for the reduction factor stands not only in the compact elegant formalism, but probably more on the rapidity of performing its evaluation. A test on a commercial processor available to date (Intel core-I7, 3.0 GHrz) shows that the integral evaluation against the hypergeometrical formulation is $\sim 10^{-4}$ s^{-1}. This translates as the possibility (to date) to generate mock catalogues for a small survey of data with about $\sim 10^4$ stars each second, against a generation of the same kinematics catalogue by numerical integration (with adaptive Runge–Kutta scheme) in about 3 hr! This result is even more striking if you distribute the computation on several processors.